Restratification at a California Current Upwelling Front, Part 1: Observations

Leah Johnson*

Brown University, Providence, RI

Craig M. Lee

Applied Physics Laboratory, Seattle, WA

Eric A. D'Asaro

Applied Physics Laboratory, Seattle, WA

Leif Thomas

Stanford University, Stanford, CA

Andrey Shcherbina

Applied Physics Laboratory, Seattle, WA

**Corresponding author address:* Department of Earth, Environmental and Planetary Sciences, Brown University, Providence, RI

E-mail: leah_johnson@brown.edu

ABSTRACT

A coordinated survey between a subsurface Lagrangian float and a ship towed Triaxus profiler obtained detailed measurements of a restratifying surface intensified front (above 30 m) within the California Current System. The survey began as down-front winds incited mixing in the boundary layer. As winds relaxed and mixing subsided, the system entered a different dynamical regime as the front developed an overturning circulation with large vertical velocities that tilted isopycnals and stratified the upper ocean within a day. The horizontal buoyancy gradient was 1.5×10^{-6} s^{-2} and associated with vorticity, divergence and strain that approached the Coriolis frequency. Estimates of vertical velocity from the Lagrangian float reached 1.2×10^{-3} m s^{-1}. These horizontal gradients and vertical velocities were consistent with submesoscale dynamics that are distinct from the classic quasi-geostrophic framework used to describe larger-scale flows. Vertical and horizontal gradients of velocity and buoyancy in the vicinity of the float revealed that sheared currents differentially advected the horizontal buoyancy gradient to increase vertical stratification. This was supported by analyses of temperature and salinity gradients that comprised the horizontal and vertical stratification. Potential vorticity was conserved during restratification at 16 m, consistent with adiabatic processes. Conversely, potential vorticity near the surface (8 m) increased, highlighting the role of friction in modulating near surface stratification. The observed increase in stratification due to these submesoscale processes was equivalent to a heat flux of 2000 W m^{-2}, an order of magnitude larger than the average observed surface heat flux of 100 W m^{-2}.

1. Introduction

The upper ocean contains rich variations in temperature (T), salinity (S), and therefore density (ρ) that change over mesoscale (100 km) and submesoscale ($0.1-10$ km) distances. Features associated with submesoscale density gradients can contain large horizontal velocity shears that induce vorticity, ζ, divergence, δ, and strain, α which are as large as the Coriolis parameter, f (Shcherbina et al. 2013). This implies Rossby numbers, $\mathrm{Ro} = \zeta/f \sim 1$, and dynamics that separate submesoscale flows from the quasi-geostrophic (QG) framework used to describe mesoscale and large-scale flows. Submesoscale features in the upper ocean have small length-scales yet strong horizontal gradients in the presence of low stratification, and therefore can undergo instabilities or interact with inertia-gravity waves (IGW) and boundary layer turbulence on timescales that are faster than mesoscale flows (Boccaletti et al. 2007; Thomas 2012, 2005; McWilliams et al. 2015). Many of the dynamics associated with submesoscale flows withdraw available potential energy stored at the front and induce large ageostrophic velocities that convert horizontal buoyancy gradients into vertical gradients, increasing vertical stratification on timescales that compete with surface radiative forcing, pointing to the importance of submesoscale fronts on upper ocean stratification. As such, the effects of subgrid scale submesoscale frontal restratification has been parameterized for course resolution models (Fox-Kemper et al. 2011), though a full understanding of these phenomena is incomplete due to the challenges in obtaining observations that capture frontal slumping.

Studies have identified an abundance of submesoscale features in influencing the upper ocean buoyancy budget (e.g. Rudnick (1999); Mahadevan et al. (2012); Hosegood et al. (2006)). Obtaining detailed observations of submesoscale processes is inherently difficult due to the need for high-resolution scalar and velocity fields ($0.1-1$ km) over a large spatial domain ($10-100$ km) within short (superinertial, i.e. less than the inertial period, $T_i = 2\pi/f$) timescales. Additionally, submesoscale flows have spatial and temporal scales comparable to unbalanced IGW, such that surveys designed to focus on submesoscale temporal and spatial scales alias wave motions. Larger mesoscale surveys of fronts are particularly designed to smooth out aliased IGW (i.e., Rudnick (1996)) and not resolve submesoscale variability. As such, a common approach is to evaluate regions with many sharp gradients within a small domain in a statistical sense (Shcherbina et al. 2013; Mahadevan et al. 2012; Thompson et al. 2016; Buckingham et al. 2016). This manuscript presents data from a Lagrangian survey that captured the evolution of a single submesoscale surface intensified front as strong ageostrophic flows, with large vertical shears and vertical velocities, tilt the front over and stratify the mixed layer (ML) within one day.

2. Data Collection

The data were collected in the California Current System (CCS) 4 – 5 August 2006, yearday (yd) 216−217, as part of the ONR Assessing the Effects of Submesoscale Ocean Parameterizations (AESOP) program. On 30 July 2006 (yd 212), northerly wind stress increased off the coast near Monterey Bay from near zero to 0.5 N m^{-2} over the course of two days. The along shore winds set up an Ekman transport offshore with an associated upwelling index of 150 (typical values range 100-200 during upwelling, `https://www.pfeg.noaa.gov/products/las.html`), and sea surface temperature (SST) that revealed cold water upwelling from the deep along the coast (Fig. 1).

An energized mesoscale field associated with the southward California Current stirred the upwelled waters with the warmer fresher surface waters offshore to create multiple smaller fronts and filaments. The front sitting at the edge of upwelled waters became the target of coordinated surveys that captured different phases of the frontal evolution. The first phase was 1−3 August

2006 (yd 213−215) as northerly winds aligned down-front continuously homogenized the upper 30 m (not discussed here). The second phase, 4−5 August 2006 (yd 216−217), occurred as winds decreased rapidly and the upper 30 m stratified. This restratification phase is the focus of this study.

During each phase, the front was surveyed by two ships simultaneously. *R/V Wecoma* performed a mesoscale survey of zonal transects set 11 km apart while towing a SeaSoar profiling vehicle (i.e., mesoscale survey, Fig. 1). Details of the mesoscale survey can be found at Pallàs-Sanz et al. (2010a,b) and Johnston et al. (2011), which characterize the vertical velocity and turbulence of the front on scales of 10−40 km. Starting 30 hr later, *R/V Melville* surveyed around a drifting Lagrangian float (D'Asaro 2003) using a Triaxus profiler, conducting a Lagrangian survey on a scale of 5 km. The mesoscale structure of the upwelling region evolved considerably between the two phases, with the front changing from a north-south orientation in phase one that developed cyclonic curvature in phase two. This was coincident with several mesoscale eddies in the surrounding regions of phase two that acted to squeeze the front together (Pallàs-Sanz et al. 2010b).

The Lagrangian float was equipped with two Seabird sensors 1.4 m apart on the top and bottom of the hull that collected measurements of pressure (P), temperature (T), and salinity (S) every 30 s which allowed for an estimation of density (ρ) and buoyancy, $b = -g\rho/\rho_o$, where g is gravitational acceleration and ρ_o is a reference density of 1024 kg m^{-3}. When neutrally buoyant, the float was designed to follow the average three-dimensional motion of the water immediately surrounding it.

The flow-through system on *R/V Melville* collected T and S at ∼5 m depth every 30 s providing a horizontal resolution of roughly 100 m. Shipboard meteorological measurements were used to estimate air-sea fluxes based on the COARE 3.5 bulk formula.

Triaxus was equipped with temperature and conductivity sensors, chlorophyll fluorometer, transmissometer, dissolved oxygen sensor, as well as 300 kHz (down-looking) and 1200 kHz (uplooking) RDI ADCPs. Triaxus profiled between 4 and 140 m depth with a vertical speed of 1 m s^{-1} and horizontal speed of roughly 3 m s^{-1}, providing horizontal resolution of 800 m near the top and bottom of the profiles and 400 m in the middle of the profiles. Shear from Triaxus ADCP was estimated using a technique similar to the inverse method for processing measurements collected with lowered ADCPs (Visbeck 2002).

Satellite SST was used to locate the front followed by an initial Triaxus transect that identified the cross-frontal structure in depth. The Lagrangian float was placed in the center of the front targeting the 23.8 kg m^{-3} isopycnal. The float's position was tracked acoustically as it was advected downstream by the frontal flow using a TrackPoint II USB system operating at 15 kHz, allowing the ship to survey around the float while towing the Triaxus profiler. The survey lasted 30 hr as the float traveled roughly 50 km along the front. During this time, the ship circled the float 31 times, taking about one hour to complete loops 3−5 km in diameter (Fig. 1).

The circular sampling pattern was well suited for calculating means and first derivatives (but not higher) of tracers and vector fields. The objective of the data processing was to project the frontal structure from Triaxus onto a transect traced by the float trajectory. Tracer and velocity data were averaged into 4 m vertical bins. Cross-frontal sections were defined by density extrema at 4 m (e.g. density maximum sets an eastern edge and density minimum sets the western edge) for a total of 62 cross-front transects. Loops were defined by two consecutive sections, and each section was included in two loops for a total of 61 loops, therefore reducing bias that may result from choice in loop definition (Fig. 2). Data in each loop and each vertical level were applied to a plane-fit, $\mathbf{y} = A\mathbf{x_1} + B\mathbf{x_2} + C$ using a least squares estimate (Deep 2005)

$$\mathbf{F} = (\mathbf{X}^T\mathbf{X})^{-1}\mathbf{X}^T\mathbf{y} \tag{1}$$

where $\mathbf{X} = (\mathbf{x_1}, \mathbf{x_2})$, denotes geographic position with $\mathbf{x_1}$ and $\mathbf{x_2}$ being the meridional and zonal distances, respectively. The variable to be fit is $\mathbf{y}$ and $\mathbf{F}$ contains the gradients (A, B) and averages (C). A 95% confidence interval (ε) associated with the least squares estimation is

$$\varepsilon = c\sqrt{(\mathbf{X}^T\mathbf{X})^{-1}(\frac{1}{m})\sum_{i=1}^{m}(\mathbf{y}-\mathbf{xF})_i^2} \tag{2}$$

where m is the number of data points in each loop to be fit and c is the t-test critical value for m. This provides an estimate of error for A and B (i.e. gradients). An example (Fig. 2b) shows a clear slope in the density field that was captured by the least squares plane fit. The results were smoothed further by averaging gradients and means for three consecutive loops $(n-1, n, n+1)$, that spanned two hours of data. (Fig. 2 a).

Gradients were used to calculate vorticity, $\zeta = \partial v/\partial x - \partial u/\partial y$, divergence, $\delta = \partial u/\partial x + \partial v/\partial y$, and strain $\alpha = \sqrt{(\partial u/\partial x - \partial v/\partial y)^2 + (\partial v/\partial x + \partial u/\partial y)^2}$ (along with propagated errors), which were essential for characterizing the submesoscale. This provided a depth vs. time (or along-front distance) view of the water surrounding the float as it was advected by the frontal flow. At times, it is more convenient to present results referenced to the frontal orientation. In this case, gradients and velocities were rotated in the direction of $\nabla_h b$ at 4 m, where positive cross-front (xf) implies down gradient and positive along-front (af) is along the direction of geostrophic shear.

Objective maps of tracer distributions were produced from the Traixus survey (Le Traon 1990; Bretherton et al. 1976) using a Gaussian covariance. Traditionally, anisotropic length-scales are chosen for mapping frontal systems. This approach was not adopted here, instead correlation length-scales were set to the approximate loop size (Lx = Ly = 5 km) to minimize along front changes due to temporal evolution. For example, as the wind stops and the float turns eastward, a 5 km swath may contain several loops and up to five hours of data, highlighting the potential influence of time-space aliasing inherent in spatially smoothing such rapidly evolving fronts.

Nonetheless, objective maps reveal essential qualitative information about the frontal structure. Results presented here use the loop method outlined above, unless noted otherwise.

The float-following reference frame allow for a Lagrangian analysis of the front, where measured rates of change can be interpreted as Lagrangian rates of change. This assumption was evaluated by estimating the change in density due to advection as $\Delta\rho_{ADV} = \int_{t_o}^{t_i} (u - u_{tri})(\partial\rho/\partial x) + (v - v_{tri})(\partial\rho/\partial y)\,dt$, where t_o is the beginning of the survey (yd 216.0), u_{tri} and v_{tri} are velocities of the survey calculated from the mean location and time of each loop, and u and v are the measured velocities of the flow at 4 m. During the survey, $\Delta\rho_{ADV}$ oscillated between ± 0.1 kg m^{-3}, with an average $\Delta\rho_{ADV} = 0.04$ kg m^{-3}. This can be compared to the $\Delta\rho$ spanned in each loop of 0.5 kg m^{-3}. Oscillations in $\Delta\rho_{ADV}$ could be attributed to the position of loop relative to a Lagrangian parcel, but on average this does not contribute significantly to the material derivative.

The assumption of Lagranian rates of change verified above is true only in layers that move in the advective frame of the float, an assumption that may not be valid in depth as the front evolves. The ability to assume Lagrangian rates of change at different depths was assessed by integrating shear in depth and time at each vertical bin, such that $d^{xf} = \int_{t_o}^{t_i} \int_{z_b}^{z_t} \left(\partial u^{xf}/\partial z\right) dz dt$, where t_o is the beginning of the survey (yd 216.0), z_t is the upper bin of Triaxus data (4 m), and z_b is the depth to be considered (Fig. 3). Therefore, d^{xf} is the distance a parcel of water at depth (z_b) traveled relative to 4 m, the closest resolved depth to the float during the time of frontal evolution (see section 4) and is a test of whether the deformation of the initially-surveyed volume is beyond the subsequent survey. For example, at yd = 216.7, a parcel of water at 20 m cannot be approximated by Lagrangian rates of change, and advective terms cannot be ignored. Similarly, d_{af} can be estimated from along-front shear (not shown), and is less than d^{xf} (consistent with section 4b). Flows near the surface (i.e., above 12 m) were approximated as Lagrangian rates of change throughout the survey.

3. Scale Resolution

Submesoscale motions are energized near the surface (Callies and Ferrari 2013; Shcherbina et al. 2013; Thompson et al. 2016) and characterized by small, sharp gradients of buoyancy and velocity with typical length scales of $0.1-10$ km and $\zeta \approx f$ that evolve on inertial timescales (T_i = $2\pi/f$ = 20.3 hr). Resolving these space and time scales present an observational challenge, yet are essential for characterizing the structure of the upper ocean. The influence of observation resolution can be readily seen by comparing tracers, velocities, and their respective gradients resolved by AVISO (Archiving, Validation and Interpretation of Satellite Oceanographic Data, `http://www.marine.copernicus.eu`; $>$100 km), the mesoscale survey (12 km) and the Lagrangian survey (5 km) (Table 1).

Objective maps of surface density from the mesoscale and Lagrangian surveys exhibit differences in intensity, structure, and position of the same front observed within 30 hours of each other (Fig. 4). The surveys aligned initially, yet deviate later as contours of the front between the two surveys diverged and wavelike features (here referred to as meanders) resolved by the Lagrangian survey were smoothed by the mesoscale survey. The $\sim$10 km wavelength meanders in the objective maps were also apparent in the raw data (not shown), and resolved in less than 10 hr by the Lagrangian survey, faster than the local inertial period, T_i = 20.3 hr. This suggests the meanders were either small scale physical features or superinertial motions and not associated with aliased tides or inertial motions. Additionally, the spatial scale of along-front variability was smaller than the objective map correlation length scales (10 - 50 km) often used for mesoscale surveys (Pallàs-Sanz et al. 2010a; Rudnick 1996).

Tracer and velocity gradients increased with higher spatial resolution (Table 1). This is seen qualitatively as isopycnals in the Lagrangian survey squeezed together (Fig. 4) compared with the mesoscale survey, consistent with a factor of two difference in $\nabla_h b$ between the surveys (Table 1). The sharper front in the Lagrangian survey was consistent with larger ζ, δ, and α, of $O(f)$ (Table 1). The fields observed by AVISO and the mesoscale survey catalog a larger-scale flow described by classic QG. This framework predicts a rapid decay in energy and vorticity in the submesoscale, associated with a velocity spectral slope of k^{-3}. The increase in gradients at smaller scales observed by the Lagrangian survey is more consistent with strong stirring and frontogenesis that sharpens lateral buoyancy gradients near the surface. This results in a shallower velocity spectral slope of k^{-2}, as previously theorized (Blumen 1978; Klein et al. 2008; Kunze 2019) and observed (Shcherbina et al. 2013; Callies and Ferrari 2013). As such, lower estimates of ζ, δ, α at larger spatial scales are not simply a result of the smoothed submesoscale field, but are ultimately associated with different dynamics. For example, strain estimated from AVISO were purely geostrophic and resulted from the mesoscale eddy field that acted to stir gradients at the surface and squeeze this front together, an essential ingredient for the submesoscale. On top of this background flow was a submesoscale α implying local processes acting to strain the front (see section 4b).

Finally, the deviation between the two surveys illustrates time space aliasing challenges of observing rapidly evolving submesoscale features and need to be considered when interpreting such data. Here, the Lagrangian survey clearly illustrates the importance of resolving small scales as the sharp gradients observed here are an important feature of submesoscale flows.

4. Frontal Evolution

a. Three stages of evolution

The initial Triaxus transect revealed the vertical structure of the surface intensified submesoscale front above a pycnocline of 30 m (Fig. 5). The entire front was broad with horizontal changes in density of 0.9 kg m^{-3} over 20 km, with evidence of sloping isopycnals deep into the interior down to 150 m. Embedded in the broad buoyancy gradient was a sharper front with a potential density anomaly difference $\Delta\sigma$ of 0.44 kg m^{-3} over 4 km between the 24−24.4 kg m^{-3} σ isopycnals with a $|\nabla_h b| = 1\times10^{-6}$ s^{-2}. This sharper portion of the front became the target of the Lagrangian survey. The entire frontal extent was not captured by the 3−5 km loop sampling pattern aimed to focus on the sharpest part of the front. The evolution of stratification can be divided into three stages. Stage 1: down-front winds, turbulent mixing, and a homogeneous boundary layer (BL). Stage 2: Low winds, diurnal warming, frontal slumping and increased stratification. Stage 3: Night-time surface cooling, increased winds, rapid near surface restratification, and float subduction (Fig. 6).

Stage 1 (yd 216−216.3): Northerly winds that began five days prior had peaked at 0.5 N m^{-2} 18 hr before the start of the survey. Stage 1 began with a 0.23 N m^{-2} down front wind stress that decreased to 0.04 N m^{-2} within 6 hr. The float was placed slightly dense (east) of the front at the 24.3 kg m^{-3} isopycnal and began traveling west towards the light side of the front. During this time, the sharpest part of the front was only partially resolved. Isopycnals in the upper 30 m were steep as the upper ocean was vertically homogeneous with strong horizontal gradients of buoyancy (Fig. 7a). For simplicity, the region above 30 m will be referred to as the mixed layer (ML), though this region was not well mixed throughout the survey.

Stage 2 (yd 216.3−216.8): The heat flux changed from cooling to warming and the wind remained less than 0.02 N m^{-2}. The float was trapped between 1−2 m such that the float's antennae was just below the surface, suggesting a decrease of turbulent mixing (Fig. 6 a, b). The float trajectory slowed down and began to veer shore-ward (east, Fig. 4). At this time, and for the remainder of the survey, the shipboard survey resolved the sharpest part of the front between 24−24.2 kg m^{-3}. During this stage, the frontal flow increased and the vertical isopycnals that defined the front squeezed closer together (Fig. 4) and began to tilt, stratifying the waters above the pycnocline (Fig. 6 b, Fig. 7, Fig. 8).

Stage 3 (yd 216.8−217.3): The heat flux changed from net warming to cooling, and the wind stress increased to 0.09 N m^{-2} and rotated to an upfront orientation (Fig. 6 c). Along-front wavelike meanders appeared in the survey and the float downwelled along isopycnals. In the classic 1-D view, night-time cooling and winds would erode the day-time stratification (e.g. Price et al. (1986)). Here, stratification in the near surface layer strengthened as warm fresh water slid over the cold salty side of the front (Fig. 7). The remainder of this manuscript aims to detail the frontal evolution. It is shown that ageostrophic circulation, associated with strong vertical shear and large vertical velocity, contributes to ML stratification.

b. Horizontal buoyancy gradient and ageostrophic shear

Horizontal buoyancy gradient was estimated using the loop method outlined in section 2 (Fig. 2) as well as using the ship underway system assuming $|\nabla b_s| = |\Delta b/\Delta s|$, where Δb and Δs are changes along the ship-track (Fig. 10). Lateral buoyancy gradients, $|\nabla b_s|$, were larger in magnitude than estimated by loop method using Triaxus at 4 m by a factor of 1.7, as gradients revealed by the flow through system (Δs ∼100 m) were not fully resolved by Triaxus with ∼800 m resolution. Lateral gradients of buoyancy from Triaxus were strongest at the surface, decreased with depth and were almost non-existent below the pycnocline (100-140 m), consistent with an increasingly surface intensified front (Fig. 9). Never throughout the survey did the front become sub-resolution (i.e., smaller than 100 m), and generally maintained a frontal width of 600 m, smaller than the mixed layer Rossby radius of deformation $L_D = NH/|f|$ of 5 km, assuming H = 30 m and N^2 averaged over stages 2−3.

Thermal wind balance was evaluated by separating the vertical shear into geostrophic $\partial \mathbf{u}^g/\partial z = \widehat{\mathbf{z}} \times (f^{-1}\nabla_h b)$ and ageostrophic ($\partial \mathbf{u}^a/\partial z = \partial \mathbf{u}/\partial z - \partial \mathbf{u}^g/\partial z$) components (Fig. 11). Here, vertical shear was rotated to the along-front (af) and across-front (xf) direction (referenced at 4 m, see section 2).

The front was only partially resolved during stage 1, yet was completely resolved by the start of stage 2. After this time, the front continued to strengthen by a factor of 2, with $|\nabla b_s|$ exceeding 2×10^{-6} s^{-2} at the surface (underway along track) within 12 hr. Throughout stages 2 and 3, the frontal structure resolved by the ship flow-through fluctuated from tight and organized to broad, and sometimes fragmented with multiple jumps in buoyancy gradient (Fig. 10). The increase in horizontal buoyancy gradient at the surface was not coincident with an increase in shear as along-front shear at 8 m remained close to zero until stage 3, when it began to approach geostrophic balance. This inhibition of total shear implies strong ageostrophic shear in the near surface that acted to oppose the frontal flow. Along-front shear at 16 m fluctuated with geostrophic shear, as ageostrophic shear, of about 0.005 s^{-1}, acted to oppose along-frontal flow. Cross-frontal shear at 16 m and 8 m behaved similarly, increasing before the onset of stage 2 and decreasing towards the end of the survey. It will be shown that this ageostrophic shear was responsible for increasing stratification at the front.

c. Stratification

Stratification in the near surface layer began to increase as turbulent mixing ceased and was coincident with day-time warming (see section 4a). Yet the evolution and distribution of stratification throughout the mixed layer points to the importance of lateral processes through frontal slumping. This is seen in the different cross-frontal structures of salinity between the beginning and end of the survey (Fig. 7) and the horizontal spreading of the 24.4 isopycnal at different depths as the front tilted over (Fig. 8). The distribution of the stratification was not uniform as deeper layers began to stratify earlier than the surface layers (Fig. 6 b, Fig. 8 a).

The lateral slumping of isopycnals was imprinted on the T and S structure of the stratification. Contributions of horizontal (frontal slumping) and vertical (i.e, turbulent mixing, vertical advection) to stratification changes can be decomposed into vertical and horizontal contributions of T and S assuming a linear equation of state, $\rho = \rho_o + \rho_o(-\alpha_T(T - T_o) + \beta(S - S_o))$, such that

$$\Delta N^2 \approx g\left[\alpha_T \frac{\partial T^v}{\partial z} + \alpha_T \frac{\partial T^h}{\partial z} - \beta \frac{\partial S^v}{\partial z} - \beta \frac{\partial S^h}{\partial z}\right], \tag{3}$$

where α_T = 2.0×10^{-4} K^{-1} is the thermal expansion coefficient for seawater and β = 7.5×10^{-4} psu^{-1} is the haline contraction coefficient for seawater. Here, $\partial T^v/\partial z$, $\partial S^v/\partial z$ are the contributions from vertical processes, and $\partial T^h/\partial z$, $\partial S^h/\partial z$ are the vertical gradients due to horizontal advection. The contribution from $\partial S/\partial z$ on N^2 was assumed to be from horizontal advection entirely (precipitation and evaporation were negligible), and therefore $\partial S^v/\partial z = 0$. Estimating the contribution from $\partial T^v/\partial z$ due to vertical processes and heat flux requires knowledge of small scale turbulence and vertical velocity, and is difficult to calculate here. Yet $\partial T^h/\partial z$ can be estimated using knowledge of the horizontal density structure through the density ratio (R),

$$R = \frac{\alpha_T \Delta T}{\beta \Delta S}. \tag{4}$$

During adiabatic slumping of isopycnals, horizontal changes in T and S are converted into vertical ones (Johnson et al. 2016). Assuming that the gradients of T and S are aligned (as in this case), that vertical changes in S are a result of horizontal advection (therefore $\partial S^h/\partial z$ is observed entirely), and R is conserved during this process, then

$$\frac{\partial T^h}{\partial z} = \frac{\beta}{\alpha_T} R^h \frac{\partial S^h}{\partial z} \tag{5}$$

where $R^h = \alpha_T \nabla_h T / \beta \nabla_h S$ (Fig. 8b). At 8 m, 80% of the vertical changes in T can be explained by $\partial T_h/\partial z$ and therefore tilted horizontal gradients, while the remaining 20% can be attributed to a combination of day-time solar warming during stage 2, vertical advection and turbulent mixing. Using $\partial T^h/\partial z$ and $\partial S^h/\partial z$ (but omitting $\partial T^v/\partial z$) in (3) provides an estimate of stratification, N^{2h}, that agrees with observed N^2 (Fig. 8 a) and support the conversion of horizontal gradients into vertical ones through frontal slumping.

Furthermore, changes in the vertical gradients of tracers as a result of differential advection by vertical shear can be quantified as

$$\frac{\mathrm{D}C_z^{ADV}}{\mathrm{D}t} = -\frac{\partial C}{\partial x}\frac{\partial u}{\partial z} - \frac{\partial C}{\partial y}\frac{\partial v}{\partial z} \tag{6}$$

for C representing tracers T, S, b. The float provided a Lagrangian reference frame for the Triaxus data such that estimates of (6) were made with the advective terms contained within the material derivative (see section 2). Vertical gradients resulting from horizontal advection, $\partial T^{ADV}/\partial z$, $\partial S^{ADV}/\partial z$ and N^{2ADV} were calculated using (6) at 8 m, where the survey was considered Lagrangian and where shear could be estimated by centered-finite-difference (Fig. 8). The ability of (6) to predict the increase in vertical gradients signifies that most changes in N^2, $\partial T/\partial z$, and $\partial S/\partial z$ were due to horizontally sheared currents advecting tracers across the front. The contribution from vertical advection, $(\partial C/\partial z)(\partial w/\partial z)$ (calculated assuming continuity), added a 10% increase in stratification to (6). This value is within error of N^{2ADV} and associated with increased uncertainty such that it was not included in (6). It is concluded that N^2 estimated from (6) and (3) in conjunction with positive cross-front ageostrophic shear present throughout the survey (Fig. 11) support the role of lateral advection of horizontal gradients for increasing stratification and is a major result of this study.

The increase in vertical stratification was used to estimate an equivalent vertical flux of buoyancy,

$$\mathscr{B}_{eq} = \frac{d}{dt}\int_{-H}^{0}\int_{-H}^{0} N^2 dz dz \tag{7}$$

Integrating total observed N^2 from H = 30 m gives $\mathscr{B}_{e_q}$ = 9.58×10^{-7} m^2 s^{-3} and a heat flux equivalent, $Q_{eq} = c_p \rho_o \mathscr{B}_{eq}/g\alpha_T$, of Q_{eq} ∼2000 W m^{-2}, where c_p is the heat capacity of seawater. This was an order of magnitude larger than the average heat fluxed onto the ocean surface during the stratification phases (2 and 3) of $Q_{avg} \sim$ 100 W m^{-2}.

d. Vorticity, divergence and strain

Vorticity, divergence, and strain were surface intensified and fluctuated throughout the survey (Fig. 9). All approached values of $O(f)$ near the surface, several times greater than values deeper below the pycnocline (100 - 140 m). In the ocean interior, inertia-gravity waves (IGW) dominate fluctuations in vorticity and divergence such that

$$\frac{\mathrm{D}\zeta}{\mathrm{D}t} \approx -(f+\zeta)\left(\frac{\partial u}{\partial x}+\frac{\partial v}{\partial y}\right). \tag{8}$$

This relationship has also been shown to exist along meanders within larger frontal systems (Bower and Rossby 1989; Thomas 2008). To assess the relationship in (8), ζ and δ were averaged at the surface (4−20 m) and depth (100−140 m) and the right hand side was integrated in time to compare with ζ assuming a lagrangian reference frame. Below the ML, where horizontal buoyancy gradient was much less than at the surface (Fig. 9), these terms oscillated with a correlation of

0.60. This oscillatory pattern at depth was decoupled from the surface (Fig. 9), where the correlation at $4-20$ m decreased to 0.17. The lack of correlation near the surface indicates that terms in the vorticity equation omitted in (8) were non-negligible in the observed flow. This can include tilting of horizontal vorticity or frictional torques, and suggest a complicated relationship between the sharp front, IGW and boundary layer dynamics.

A background strain field estimated from the mesoscale survey to be $0.3f$ (Pallàs-Sanz et al. (2010b)) was attributed to eddies in the surrounding mesoscale field. On top of this background strain, $O(f)$ strain was resolved by the Lagrangian survey (Table 1) that was particular to the local dynamics around the front, and was not captured by the mesoscale survey or AVISO. The influence of this strain field on ∇b_h is captured by the frontogenetic tendency equation associated with horizontal advection (Hoskins 1982)

$$F_{hadv} = \frac{1}{2}\frac{\mathrm{D}|\nabla_h b|^2}{\mathrm{D}t}\bigg|_{hadv} = \left(-\frac{\partial b}{\partial x}\nabla_h u - \frac{\partial b}{\partial y}\nabla_h v\right)\cdot\nabla_h b \qquad (9)$$

that includes both the geostrophic and ageostrophic component of the flow (Fig. 12). F_{hadv} was near zero during stage one. After wind forcing ceased, F_{hadv} fluctuated between frontogenetic and frontolytic between yd $216.2-216.6$. During this time, $\nabla_h b$ steadily increased (Fig. 9). The largest values of F_{hadv} at the end of stage 2 and beginning of stage 3 were simultaneous with strong $\nabla_h b$. Although there was consistency between positive frontogenetic tendency and an increase in frontal strength, the tendency of $\nabla_h b$ cannot be explained by integrating (9) in time, including the increase at the beginning of stage 2 or the deterioration $\nabla_h b$ after yd 217. Large errors in F_{hadv} are expected with the multiple derivatives needed to compute (9), and may not represent the true F_{hadv} of the front. Additionally, turbulence and vertical velocity may induce a frontal response (Gula et al. 2014), that are not resolved here and can be frontolytic and counteract F_{hadv}.

The classic frontogenesis problem of Hoskins and Bretherton (1972) assumes the advection of momentum by the ageostrophic flow is negligible following the semigeostrophic approximation. Here, frontogenesis and frontal sharpening occurred in the presence of strong divergence as well as large ageostrophic, cross front shears. Departures from classic frontogenesis have been explored in context of submesoscale fronts by Shakespeare and Taylor (2013) and Barkan et al. (2019), suggesting a regime of submesoscale frontogenesis in addition to that induced by external strain. In particular, Barkan et al. (2019) explored frontogenesis in the presence of large convergence and found cross frontal flows to have a reinforcing role on the frontogenetic sharpening rate. A complete discussion of this observed front in context of different frontogenetic frameworks would require isolating the relative contributions of the geostrophic and ageostrophic flows in the frontogenetic function, which cannot be done in this data set (see section 4b). Nonetheless, the ageostrophic cross front shears along with the increase in strain and divergence resolved by the Lagrangian survey compared to the mesoscale survey and Aviso (Table 1) are characteristics consistent with submesoscale frontogenesis.

The different horizontal gradients resolved by the mesoscale survey and the Lagrangian survey lead to contrasting interpretations of fronotgenesis. In particular, the sharpening of the front and positive F_{hadv} observed by the Lagrangian survey was opposite than predicted by the mesoscale survey (estimated using a generalized omega equation, Pallàs-Sanz et al. (2010a)) which deduced a frontolytic circulation resulting from the frontal curvature and associated deformation field. Frontogenesis was a key part of the Lagrangian survey as it strengthened the horizontal buoyancy gradient and therefore the amount of stratification from horizontal slumping (i.e. through (6)).

e. Vertical Velocity

The float measured pressure and hence depth every 30 s, allowing for direct measurements of vertical velocity. To minimize high-frequency motions from the float, a LOESS was applied to 30 min of the float's vertical position to obtain an estimate of vertical velocity. During stages 1 and 2 the float was ballasted buoyant and adjusted again before stage 3. During stage 1, the vertical velocity and low stratification were consistent with boundary layer turbulence. After winds decreased and boundary layer mixing subsided (stages 2 and 3), the float observed four downwelling events between stratified layers (I−IV on Fig. 13), where the float trajectory implied a downwelling from the dense side of the front under the lighter side of the front (Fig. 13 c). The largest of these events was III and is discussed in detail.

At yd 216.8 the float's horizontal velocity slowed as it began to downwell at 1.3×10^{-3} mm s^{-1} (120 m d^{-1}) across and under the warm side of the front (Fig. 7, Fig. 13 a, c). In the upper 4 m, the float traveled trough changes in density and stratification, suggesting the initial sinking was neither purely turbulent nor purely adiabatic. Below 4 m, the float's density remained constant as it continued to downwell at $w = 0.7\times10^{-3}$ mm s^{-1} (60 m d^{-1}). During this time, the float was caught in an anticyclonic flow as it wrapped westward (Fig. 13a). Throughout the meander, the float's vertical velocity slowed, nearing zero. At yd 217 the float was automatically set to profile and no longer tracks the vertical velocity of the water.

The downwelling of the float in III occurred on the upstream side of cyclonic flow (Fig. 13a), with $\zeta > 0$ and $\delta < 0$. This geometry of downwelling was consistent with frontal subduction observed and modelled previously within larger frontal systems (e.g. Bower and Rossby (1989); Lindstrom et al. (1997); Spall (1997)). Here, the subduction occurred in the presence of large convergences and a cyclonic flow that could be tied to either along-front variability or IGW, both which share similar space and time scales and are therefore complicated to separate.

The contributions of IGW and frontal dynamics could be achieved theoretically by solving the Eliassen-Sawyer (ES) equation or the omega equation to obtain the balanced ASC. For example, Mahadevan and Tandon (2006) used numerical simulation fields to solve the omega equation and obtain the contribution of balanced dynamics to the total vertical velocity determined by the simulation. The residual vertical velocity was then attributed to unbalanced motions. The ES or omega formulation has been implemented in many mesoscale observations to obtain ACS (e.g. ES - Thomas (2008), omega equation - Rudnick (1996), generalized omega equation - Pallàs-Sanz et al. (2010a)). A challenge in this set of observations lies in capturing the nuanced structure of buoyancy and momentum needed to constrain a submesoscale frontal ASC using these techniques. This was made unfeasible as the Triaxus survey resolved a narrow and shallow portion of the front only. The unconstrained boundary conditions influence, and therefore add uncertainty, to the solution. Additionally, the along front curvature, which can play an essential role in a deformation field, may be aliased IGW and difficult to interpret. The cross frontal extent of the Lagrangian survey is an example of the trade-off between spatial coverage and temporal aliasing, a balance that is paramount to observations in the submesoscale regime. The inability to obtain a cross frontal structure of buoyancy and velocity on a timescale that minimizes temporal aliasing presents a limitation on inversion techniques for submesoscale observations. Any assumptions to approximate these fields would obfuscate the interpretation of the submesoscale ASC.

In lieu of mesoscale inversion techniques, the divergent flow field was used to estimate vertical velocity (assuming a rigid lid $w = 0$)

$$w_\delta = \int_{-8\mathrm{m}}^{0\mathrm{m}} \delta dz \tag{10}$$

with a bottom limit (8 m) set by the vertical extent of the float. During III, w_δ predicted downwelling, but greatly underestimated the vertical velocities experienced by the float (Fig. 13 b). This suggests a highly localized region of downwelling at the front that could not be resolved by the 5 km distances used to calculate δ. This highly localized vertical velocity is reminiscent of the increase in ζ, α, and δ at smaller scales presented in Table 1, and is a feature of the submesoscale in general.

Finally, the $T-S$ gradients that comprised the vertical stratification measured by the float were similar to the $T-S$ gradients of the horizontal stratification measured by Triaxus and the ship flow-through during the time of subduction (yd 216.8−217, Fig. 13 d), consistent with budgets in section 4c. The classic paper by Iselin (1939) recognized the relationship between horizontal water mass changes in the winter ML and vertical water mass changes in the thermocline as an indicator of wintertime subduction of surface waters into the interior. The horizontal and vertical $T-S$ relationship observed by the Lagrangian survey captured this same signature of subduction, yet are a result of different dynamics occurring on smaller length and faster temporal scales.

f. Potential vorticity

Ertel potential vorticity (PV)

$$q = (f\hat{\mathbf{z}} + \nabla \times \mathbf{u}) \cdot \nabla b \tag{11}$$

is a dynamically relevant tracer and is conserved following fluid parcels unless subject to non-conservative forces or diabatic processes (Marshall and Nurser 1992), such that

$$\frac{\mathrm{D}q}{\mathrm{D}t} = 0 \tag{12}$$

In the absence of horizontal density gradients, PV conservation implies that the vertical term of PV

$$q_v = (f + \zeta)N^2 \tag{13}$$

does not change following a fluid parcel. Neglecting derivatives in vertical velocity, the horizontal term is

$$q_h = \frac{\partial u}{\partial z}\frac{\partial b}{\partial y} - \frac{\partial v}{\partial z}\frac{\partial b}{\partial x} \tag{14}$$

Near fronts, the horizontal term becomes leading order and an important contributor to a fluid parcel's PV. If the shear is purely geostrophic, then the horizontal term becomes

$$q_{hg} = -\frac{|\nabla_h b|^2}{f} \tag{15}$$

a negative definite quantity in the Northern Hemisphere. The presence of ageostrophic shears and surface forcing, which are often crucial to momentum and buoyancy budgets in the ML, can influence both q_v and q_h. The evolution of PV estimated from this survey (Fig. 14) exhibited two different stories: a deeper layer (16 m) where PV was conserved (~ 0), lying underneath a surface layer of increasing PV (8 m). The components of PV following the float were used to describe this evolution. Thomas (2008) laid out three conditions under which PV at fronts can have near zero PV

i. Vertically mixed momentum and buoyancy to create $N^2 = 0$ and $|\mathbf{u}_z| = 0$;

ii. Vortically low PV as $\zeta \rightarrow -f$ and $|\nabla_h b| = 0$

iii. Baroclinically low PV $q_h \rightarrow -q_v$

In the beginning of the survey, BL turbulence homogenized tracers and momentum throughout the ML. This caused a lack of shear and stratification that resulted in close to zero q_v and q_h as in (i).

Both terms were smaller than the value associated with geostrophic balance and consistent with large ageostrophic shears (Fig. 11).

At the start of stage 2, PV throughout the upper 30 m evolved differently. Deeper in the ML (16 m), isopycnals began to tilt, causing the once homogeneous ML to stratify and q_v to increase. The tilting of isopycnals (e.g., Fig. 8a) was accompanied by an increase in both horizontal buoyancy gradient and vertical shear such that q_h compensated q_v as in (iii). This resulted in near zero PV through yd 216.7 (at 16 m) after which advective terms may become important and interpretation is less clear (see section 2, Fig. 3). At this depth (16 m), changes in q_v and q_h tracked $|\nabla_h b/f|$ (Fig. 14), demonstrating the balanced state of the front during this time.

PV conservation was not evident in the near surface layer (8 m). During stage 2, q_v increased with stratification. During stage 3, q_v remained level and decreased slightly as the increase in stratification at the end of the survey was offset by a decrease in ζ and consistent with the anticyclonic circulation. Unlike the middle of the ML (16 m), changes in q_v at 8 m were not balanced by q_h. Horizontal buoyancy gradient increased during stage 2, yet strong upfront shear inhibited development of q_h such that q_h did not approach q_{hg}. Furthermore, the presence of ageostrophic cross-front shear encouraged frontal tilting (Fig. 8) and increased stratification (and therefore q_v), but did not contribute to q_h because the along-front buoyancy gradient was, by definition, zero. In summary, cross-front shear resulted in an increase in q_v through N^2, while along-front ageostrophic shear inhibited q_h, such that q_v and q_h did not balance and total q increased. This reveals the importance of ageostrophic shear in modulating PV at 8 m.

The relationship between horizontal and vertical PV is an important part of understanding submesoscale frontal dynamics as was captured by the loop method here. This balance was not maintained by the objectively mapped fields that underestimated q_h and therefore predicted an increase in total q at 16 m. The difference in PV between the loop method and the objective maps highlights the challenge in estimating and interpreting observed PV at submesoscale fronts, where the horizontal component of PV plays an essential role and therefore needs to be resolved.

5. Discussion

A Lagrangian survey, processed on spatial scales of 5 km (diameter of the looped survey pattern) and temporal scales of 2 hours (time-span contained in one data point), revealed surface intensified gradients of buoyancy and velocity as well as vertical velocities that were larger than the accompanying mesoscale survey or estimates from AVISO (Table 1, Fig. 1, Fig. 4). Horizontal gradient magnitudes were largest near the surface and decayed with depth. These patterns are not consistent with a classic QG framework, but instead are signatures of the submesoscale range. Flows approaching Ro = $\zeta/f \sim 1$, are better described by a semi-geostrophic framework and result in shallower velocity spectral slopes of $\sim k^{-2}$ at high wavenumbers as found in model studies that resolve the submesoscale (Capet et al. 2008; Klein et al. 2008). This is also consistent with $\sim k^{-2}$ spectral slopes observed near the surface that are not predicted by estimates using satellite altimetry or found deeper below the ML (Shcherbina et al. 2013; Callies and Ferrari 2013). Spectral slopes of $\sim k^{-2}$ result from a velocity field influenced by frontogenesis, instabilities, and large ageostrophic motions, all which manifest signatures at this front. Here, the large values of vorticity, divergence and strain may result from a combination of frontal dynamics and IGWs within the ML. These balanced and unbalanced velocities are intertwined in the ML, yet are decoupled from an internal wave field observed at depth as gradients of buoyancy and velocity decay below the pycnocline.

The coordinated mesoscale and Lagrangian surveys provided a nested view of this submesoscale front. Yet the two surveys document different phenomena. The mesoscale survey described by Pallàs-Sanz et al. (2010a) and Johnston et al. (2011) spanned 130 km meridionally, 70 km zonally and 16 - 355 m vertically. In contrast, the Lagrangian survey spanned 5 km across the front and 50 km in the along front direction. The Lagrangian survey was located in the northwest quadrant of the mesoscale survey and overlapped with four Seasoar tracks that were set 11 km apart (Fig. 4). Pallàs-Sanz et al. (2010b) and Johnston et al. (2011) used a generalized omega equation and the classic QG omega equation, respectively, to discuss the frontal response to deformation fields and it's impact on the turbulence and tracer distribution at the front. These results showed that strong ASC developed as a response to the external deformation field (Pallàs-Sanz et al. 2010a) as surrounding mesoscale eddies strain the front. Additionally, Johnston et al. (2011) mapped a deep chlorophyll maximum around 100 m (a feature seen deep in the Triaxus data as well), consistent with strong downwelling on the edge of the neighboring eddy. An ASC derived from the mesoscale fields using a generalized omega equation approach (Pallàs-Sanz et al. 2010a), predicts frontolysis due to ageostrophic velocities from the frontal curvature in the domain of the Lagrangian survey. Conversely, the Lagrangian survey documented frontal strengthening simultaneous with ageostrophic cross-frontal shear, float subduction and tilting isopycnals, consistent with a restratifying ASC, though not formally quantified here. The frontal curvature deviates between the Lagrangian and the mesoscale survey (Fig. 4), a result of the rapidly evolving and tilting submesoscale front and therefore is not comparable to the curve in the mesoscale survey.

The difference in frontogenesis between the two surveys reiterate the multiple scales of processes that occur in a single region and presents an inconsistency with the near surface frontal dynamics and those happening deeper (i.e. 5-20 m vs. 20-100 m). The mesoscale ASC was calculated using an objectively mapped buoyancy and flow field with decorrelation lengths comparable to the entire extent of the Lagrangian survey and a rigid lid assumption that set $w = 0$ at 16 m. It therefore was not targeted to isolate the large near surface vertical velocities, high shears, or frontal restratification observed in the upper 10 m of the Lagrangian survey. The near surface frontogenesis observed by the Lagrangian survey is reminiscent of the submesoscale frontogenesis discussed in Shakespeare and Taylor (2013) and Barkan et al. (2019), distinctly different from those explored in the classic or generalized omega equations. The mesoscale and Lagrangian surveys each resolved different frontogenetic regimes, yet neither survey captured the processes occurring on multiple scales simultaneously.

Satellite SST (Fig. 1) revealed filaments and meanders along the upwelling front suggesting along front variability. Furthermore, the Lagrangian survey observed large horizontal gradients, frontogenetic tendency, vertical velocities and possible meandering structures consistent with frontal baroclinic instabilities (mixed layer instabilities, MLI, (Boccaletti et al. 2007)). MLI baroclinic waves grow with length-scales that follow L_D (here, 5 km), and a timescale of days. These waves release available potential energy by converting horizontal stratification into a vertical one. While the along-front variability of $5-10$ km (Fig. 4) may be consistent with growing baroclinic waves, the rapid stratification of this front (i.e. less than the inertial period, T_i = 20.3 hr) presents an inconsistency between the observations and MLI theory. Additionally, it was impossible to isolate the physical along-front variability from temporal IGW. Therefore the role of MLI remains illusive.

A characteristic of this front was the non-conservation of PV near the surface as the ageostrophic shear impeded growth of the q_h while stratification (q_v) increased. Surface friction due to wind driven or geostrophic stress can modulate shear and therefore PV. The role of wind driven and geostrophic shear at fronts are usually explored in steady state (Thomas and Lee 2005; Thompson 2000; Cronin and Kessler 2009; Wenegrat and McPhaden 2015; McWilliams et al. 2015) and therefore assuming subinertial timescales. Previous observations have isolated ageostrophic shears in the presence of geostrophic currents on timescales of days (Lee and Eriksen 1996) and months (Cronin and Kessler 2009) that satisfy the Ekman relation, rotating right and decreasing with depth.

Ageostrophic shear averaged throughout this survey reveal a similar rotation profile in depth (not shown). Not surprisingly, this Ekman like pattern is absent in instantaneous profiles. Additionally, using average shear in place of instantaneous shear in (6) underestimates stratification by 60%. These discrepancies highlight the importance of unsteady forcing and superinertial fluctuations in shear for increasing stratification at this front and modulating PV near the surface.

6. Conclusion

A highly detailed process study captured the restratification of a surface intensified submesoscale front in the California Current System on superinertial timescales. The survey pattern allowed for reliable calculation of vertical and horizontal gradients in a Lagrangian framework and showed that vertical gradients in b, T, and S were a result of differential advection of horizontal gradients by ageostrophic cross front vertical shear. The increase in stratification resulting from frontal slumping was equivalent to a flux of buoyancy of 2000 W m $^{-2}$, compared to an average heat flux of 100 W m^{-2} during the restratification phases (2 and 3). Strong ageostrophic circulation was accompanied by vertical velocities reaching 1.3×10^{-3} mm s^{-1} (120 m d^{-1}), as well as ζ, δ and α that approached the Coriolis frequency. These features are a departure from the classic QG framework and are characteristic of a submesoscale regime. Frontogenesis and the strengthening of the horizontal buoyancy gradient played a key role in frontal evolution, transferring energy to smaller scales (through frontal sharpening) and influencing the upper ocean buoyancy budget (by increasing stratification due to horizontal slumping). The increase in stratification was accompanied by an increase in the vertical component of PV. In the middle of the ML (16 m), the increase in vertical PV was balanced by decreases in horizontal PV and evidence of PV conservation. This relationship did not exist near the surface (8 m), as vertical PV increased without compensation from the horizontal component. The results presented here point to the importance of near surface Ekman dynamics and frontal instabilities, which are explored in a companion manuscript combining these observations with idealized models.

Acknowledgments. This work was supported by Office of Naval Research Grants N00014-05-1-0329 and N00014-09-1-0266. We thank Daniel Rudnick and Enric Pallàs-Sanz for sharing data from the mesoscale survey that complimented and extended this analysis. Insightful comments by Eric Kunze and two anonymous reviewers greatly improved the manuscript.

References

Barkan, R., M. J. Molemaker, K. Srinivasan, J. C. McWilliams, and E. A. D'Asaro, 2019: The Role of Horizontal Divergence in Submesoscale Frontogenesis. *Journal of Physical Oceanography*, **49 (6)**, 1593–1618, doi:10.1175/JPO-D-18-0162.1, URL https://doi.org/10.1175/JPO-D-18-0162.1.

Blumen, W., 1978: Uniform Potential Vorticity Flow: Part I. Theory of Wave Interactions and Two-Dimensional Turbulence. *Journal of the Atmospheric Sciences*, **35 (5)**, 774–783, doi:10.1175/1520-0469(1978)035⟨0774:UPVFPI⟩2.0.CO;2, URL http://journals.ametsoc.org/doi/abs/10.1175/1520-0469{\%}281978{\%}29035{\%}3C0774{\%}3AUPVFPI{\%}3E2.0.CO{\%}3B2.

Boccaletti, G., R. Ferrari, and B. Fox-Kemper, 2007: Mixed Layer Instabilities and Restratification. *Journal of Physical Oceanography*, **37 (9)**, 2228–2250, doi:10.1175/JPO3101.1, URL https://doi.org/10.1175/JPO3101.1http://journals.ametsoc.org/doi/abs/10.1175/JPO3101.1.

Bower, A. S., and T. Rossby, 1989: Evidence of Cross-Frontal Exchange Processes in the Gulf Stream Based on Isopycnal RAFOS Float Data. *Journal of Physical Oceanography*, **19 (9)**, 1177–1190, doi:10.1175/1520-0485(1989)019⟨1177:EOCFEP⟩2.0.CO;2, URL https://doi.org/10.1175/1520-0485(1989)019{\%}3C1177:EOCFEP{\%}3E2.0.CO2http://journals.ametsoc.org/doi/abs/10.1175/1520-0485{\%}281989{\%}29019{\%}3C1177{\%}3AEOCFEP{\%}3E2.0.CO{\%}3B2.

Bretherton, F. P., R. E. Davis, and C. Fandry, 1976: A technique for objective analysis and design of oceanographic experiments applied to MODE-73. *Deep Sea Research and Oceanographic Abstracts*, **23 (7)**, 559–582, doi:10.1016/0011-7471(76)90001-2, URL http://www.sciencedirect.com/science/article/pii/0011747176900012https://linkinghub.elsevier.com/retrieve/pii/0011747176900012.

Buckingham, C. E., and Coauthors, 2016: Seasonality of submesoscale flows in the ocean surface boundary layer. *Geophysical Research Letters*, **43 (5)**, 2118–2126, doi:10.1002/2016GL068009, URL https://onlinelibrary.wiley.com/doi/abs/10.1002/2016GL068009.

Callies, J., and R. Ferrari, 2013: Interpreting Energy and Tracer Spectra of Upper-Ocean Turbulence in the Submesoscale Range (1200 km). *Journal of Physical Oceanography*, **43 (11)**, 2456–2474, doi:10.1175/JPO-D-13-063.1, URL https://doi.org/10.1175/JPO-D-13-063.1http://journals.ametsoc.org/doi/abs/10.1175/JPO-D-13-063.1.

Capet, X., J. C. McWilliams, M. J. Molemaker, and A. F. Shchepetkin, 2008: Mesoscale to Submesoscale Transition in the California Current System. Part I: Flow Structure, Eddy Flux, and Observational Tests. *Journal of Physical Oceanography*, **38 (1)**, 29–43, doi:10.1175/2007JPO3671.1, URL https://doi.org/10.1175/2007JPO3671.1http://journals.ametsoc.org/doi/abs/10.1175/2007JPO3671.1.

Cronin, M. F., and W. S. Kessler, 2009: Near-Surface Shear Flow in the Tropical Pacific Cold Tongue Front*. *Journal of Physical Oceanography*, **39 (5)**, 1200–1215, doi:10.1175/

2008JPO4064.1, URL https://doi.org/10.1175/2008JPO4064.1http://journals.ametsoc.org/doi/abs/10.1175/2008JPO4064.1.

D'Asaro, E. A., 2003: Performance of Autonomous Lagrangian Floats. *Journal of Atmospheric and Oceanic Technology*, **20 (6)**, 896–911, doi:10.1175/1520-0426(2003)020⟨0896:POALF⟩2.0.CO;2, URL http://journals.ametsoc.org/doi/abs/10.1175/1520-0426{\%}282003{\%}29020{\%}3C0896{\%}3APOALF{\%}3E2.0.CO{\%}3B2.

Deep, R., 2005: *Probability and Statistics : With Integrated Software Routines*. Elsevier Science & Technology, Burlington, UNITED STATES, URL http://ebookcentral.proquest.com/lib/brown/detail.action?docID=294324.

Fox-Kemper, B., and Coauthors, 2011: Parameterization of mixed layer eddies. III: Implementation and impact in global ocean climate simulations. *Ocean Modelling*, **39 (1-2)**, 61–78, doi:10.1016/j.ocemod.2010.09.002, URL https://linkinghub.elsevier.com/retrieve/pii/S1463500310001290.

Gula, J., M. J. Molemaker, and J. C. McWilliams, 2014: Submesoscale Cold Filaments in the Gulf Stream. *Journal of Physical Oceanography*, **44 (10)**, 2617–2643, doi:10.1175/JPO-D-14-0029.1, URL http://journals.ametsoc.org/doi/abs/10.1175/JPO-D-14-0029.1.

Hosegood, P., M. C. Gregg, and M. H. Alford, 2006: Sub-mesoscale lateral density structure in the oceanic surface mixed layer. *Geophysical Research Letters*, **33 (22)**, L22 604, doi:10.1029/2006GL026797, URL https://doi.org/10.1029/2006GL026797http://doi.wiley.com/10.1029/2006GL026797.

Hoskins, B. J., 1982: The Mathematical Theory of Frontogenesis. *Annual Review of Fluid Mechanics*, **14 (1)**, 131–151, doi:10.1146/annurev.fl.14.010182.001023, URL https://doi.org/10.1146/annurev.fl.14.010182.001023http://www.annualreviews.org/doi/10.1146/annurev.fl.14.010182.001023.

Hoskins, B. J., and F. P. Bretherton, 1972: Atmospheric frontogenesis models: Mathematical formulation and solution. *Journal of the Atmospheric Sciences*, **29 (1)**, 11–37, doi:10.1175/1520-0469(1972)029⟨0011:AFMMFA⟩2.0.CO;2, URL https://doi.org/10.1175/1520-0469(1972)029⟨0011:AFMMFA⟩2.0.CO;2, https://doi.org/10.1175/1520-0469(1972)029⟨0011:AFMMFA⟩2.0.CO;2.

Iselin, C. O., 1939: The influence of vertical and lateral turbulence on the characteristics of the waters at mid-depths. *Transactions, American Geophysical Union*, **20 (3)**, 414, doi:10.1029/TR020i003p00414, URL http://doi.wiley.com/10.1029/TR020i003p00414.

Johnson, L., C. M. Lee, and E. A. D'Asaro, 2016: Global Estimates of Lateral Springtime Restratification. *Journal of Physical Oceanography*, **46 (5)**, 1555–1573, doi:10.1175/JPO-D-15-0163.1, URL https://doi.org/10.1175/JPO-D-15-0163.1http://journals.ametsoc.org/doi/10.1175/JPO-D-15-0163.1.

Johnston, T. M. S., D. L. Rudnick, and E. Pallàs-Sanz, 2011: Elevated mixing at a front. *Journal of Geophysical Research*, **116 (C11)**, C11 033, doi:10.1029/2011JC007192, URL https://doi.org/10.1029/2011JC007192http://doi.wiley.com/10.1029/2011JC007192.

Klein, P., B. L. Hua, G. Lapeyre, X. Capet, S. Le Gentil, and H. Sasaki, 2008: Upper Ocean Turbulence from High-Resolution 3D Simulations. *Journal of Physical Oceanography*, **38 (8)**, 1748–1763, doi:10.1175/2007JPO3773.1, URL http://journals.ametsoc.org/doi/abs/10.1175/2007JPO3773.1.

Kunze, E., 2019: A Unified Model Spectrum for Anisotropic Stratified and Isotropic Turbulence in the Ocean and Atmosphere. *Journal of Physical Oceanography*, **49 (2)**, 385–407, doi:10.1175/JPO-D-18-0092.1, URL https://doi.org/10.1175/JPO-D-18-0092.1http://journals.ametsoc.org/doi/10.1175/JPO-D-18-0092.1.

Le Traon, P. Y., 1990: A method for optimal analysis of fields with spatially variable mean. *Journal of Geophysical Research*, **95 (C8)**, 13 543, doi:10.1029/JC095iC08p13543, URL http://doi.wiley.com/10.1029/JC095iC08p13543.

Lee, C. M., and C. C. Eriksen, 1996: The Subinertial Momentum Balance of the North Atlantic Subtropical Convergence Zone. *Journal of Physical Oceanography*, **26 (9)**, 1690–1704, doi:10.1175/1520-0485(1996)026⟨1690:TSMBOT⟩2.0.CO;2, URL https://doi.org/10.1175/1520-0485(1996)026{\%}3C1690:TSMBOT{\%}3E2.0.COhttp://0.0.0.2http://journals.ametsoc.org/doi/abs/10.1175/1520-0485{\%}281996{\%}29026{\%}3C1690{\%}3ATSMBOT{\%}3E2.0.CO{\%}3B2.

Lindstrom, S. S., X. Qian, and D. R. Watts, 1997: Vertical motion in the Gulf Stream and its relation to meanders. *Journal of Geophysical Research: Oceans*, **102 (C4)**, 8485–8503, doi:10.1029/96JC03498, URL http://doi.wiley.com/10.1029/96JC03498.

Mahadevan, A., E. D'Asaro, C. Lee, and M. J. Perry, 2012: Eddy-Driven Stratification Initiates North Atlantic Spring Phytoplankton Blooms. *Science*, **337 (6090)**, 54–58, doi:10.1126/science.1218740, URL http://science.sciencemag.org/content/337/6090/54http://www.sciencemag.org/lookup/doi/10.1126/science.1218740.

Mahadevan, A., and A. Tandon, 2006: An analysis of mechanisms for submesoscale vertical motion at ocean fronts. *Ocean Modelling*, **14 (3-4)**, 241–256, doi:10.1016/j.ocemod.2006.05.006, URL https://linkinghub.elsevier.com/retrieve/pii/S1463500306000540.

Marshall, J. C., and A. J. G. Nurser, 1992: Fluid Dynamics of Oceanic Thermocline Ventilation. *Journal of Physical Oceanography*, **22 (6)**, 583–595, doi:10.1175/1520-0485(1992)022⟨0583:FDOOTV⟩2.0.CO;2, URL https://doi.org/10.1175/1520-0485(1992)022{\%}3C0583:FDOOTV{\%}3E2.0.CO2http://journals.ametsoc.org/doi/abs/10.1175/1520-0485{\%}281992{\%}29022{\%}3C0583{\%}3AFDOOTV{\%}3E2.0.CO{\%}3B2.

McWilliams, J. C., J. Gula, M. J. Molemaker, L. Renault, and A. F. Shchepetkin, 2015: Filament Frontogenesis by Boundary Layer Turbulence. *Journal of Physical Oceanography*, **45 (8)**, 1988–2005, doi:10.1175/JPO-D-14-0211.1, URL https://doi.org/10.1175/JPO-D-14-0211.1http://journals.ametsoc.org/doi/10.1175/JPO-D-14-0211.1.

Pallàs-Sanz, E., T. M. S. Johnston, and D. L. Rudnick, 2010a: Frontal dynamics in a California Current System shallow front: 1. Frontal processes and tracer structure. *Journal of Geophysical Research*, **115 (C12)**, C12 067, doi:10.1029/2009JC006032, URL https://doi.org/10.1029/2009JC006032http://doi.wiley.com/10.1029/2009JC006032.

Pallàs-Sanz, E., T. M. S. Johnston, and D. L. Rudnick, 2010b: Frontal dynamics in a California Current System shallow front: 2. Mesoscale vertical velocity. *Journal of Geophysical Research*, **115 (C12)**, C12 068, doi:10.1029/2010JC006474, URL https://doi.org/10.1029/2010JC006474http://doi.wiley.com/10.1029/2010JC006474.

Price, J. F., R. A. Weller, and R. Pinkel, 1986: Diurnal cycling: Observations and models of the upper ocean response to diurnal heating, cooling, and wind mixing. *Journal of Geophysical Research*, **91 (C7)**, 8411, doi:10.1029/JC091iC07p08411, URL https://doi.org/10.1029/JC091iC07p08411http://doi.wiley.com/10.1029/JC091iC07p08411.

Rudnick, D. L., 1996: Intensive surveys of the Azores Front: 2. Inferring the geostrophic and vertical velocity fields. *Journal of Geophysical Research: Oceans*, **101 (C7)**, 16 291–

16 303, doi:10.1029/96JC01144, URL https://doi.org/10.1029/96JC01144http://doi.wiley.com/10.1029/96JC01144.

Rudnick, D. L., 1999: Compensation of Horizontal Temperature and Salinity Gradients in the Ocean Mixed Layer. *Science*, **283 (5401)**, 526–529, doi:10.1126/science.283.5401.526, URL http://science.sciencemag.org/content/283/5401/526http://www.sciencemag.org/cgi/doi/10.1126/science.283.5401.526.

Shakespeare, C. J., and J. R. Taylor, 2013: A generalized mathematical model of geostrophic adjustment and frontogenesis: uniform potential vorticity. *Journal of Fluid Mechanics*, **736**, 366–413, doi:DOI:10.1017/jfm.2013.526, URL https://www.cambridge.org/core/article/generalized-mathematical-model-of-geostrophic-adjustment-and-frontogenesis-uniform-potential-vortic 809C48C22ED63CE88E1CCAF715D22343.

Shcherbina, A. Y., E. A. D'Asaro, C. M. Lee, J. M. Klymak, M. J. Molemaker, and J. C. McWilliams, 2013: Statistics of vertical vorticity, divergence, and strain in a developed submesoscale turbulence field. *Geophysical Research Letters*, **40 (17)**, 4706–4711, doi:10.1002/grl.50919, URL https://doi.org/10.1002/grl.50919http://doi.wiley.com/10.1002/grl.50919.

Spall, M. A., 1997: Baroclinic Jets in Confluent Flow*. *Journal of Physical Oceanography*, **27 (6)**, 1054–1071, doi:10.1175/1520-0485(1997)027⟨1054:BJICF⟩2.0.CO;2, URL https://doi.org/10.1175/1520-0485(1997)027{\%}3C1054:BJICF{\%}3E2.0.CO2http://journals.ametsoc.org/doi/abs/10.1175/1520-0485{\%}281997{\%}29027{\%}3C1054{\%}3ABJICF{\%}3E2.0.CO{\%}3B2.

Thomas, L. N., 2005: Destruction of Potential Vorticity by Winds. *Journal of Physical Oceanography*, **35 (12)**, 2457–2466, doi:10.1175/JPO2830.1, URL https://doi.org/10.1175/JPO2830.1http://journals.ametsoc.org/doi/abs/10.1175/JPO2830.1.

Thomas, L. N., 2008: Formation of intrathermocline eddies at ocean fronts by wind-driven destruction of potential vorticity. *Dynamics of Atmospheres and Oceans*, **45 (3-4)**, 252–273, doi:10.1016/j.dynatmoce.2008.02.002, URL https://www.sciencedirect.com/science/article/pii/S0377026508000353https://linkinghub.elsevier.com/retrieve/pii/S0377026508000353.

Thomas, L. N., 2012: On the effects of frontogenetic strain on symmetric instability and inertiagravity waves. *Journal of Fluid Mechanics*, **711**, 620–640, doi:10.1017/jfm.2012.416, URL https://www.cambridge.org/core/article/on-the-effects-of-frontogenetic-strain-on-symmetric-instability-and-inertiagravity-waves/432906BD32BE1674C7F9FA04680F0F8Ehttps://www.cambridge.org/core/product/identifier/S0022112012004168/type/journal{_}article.

Thomas, L. N., and C. M. Lee, 2005: Intensification of Ocean Fronts by Down-Front Winds. *Journal of Physical Oceanography*, **35 (6)**, 1086–1102, doi:10.1175/JPO2737.1, URL https://doi.org/10.1175/JPO2737.1http://journals.ametsoc.org/doi/abs/10.1175/JPO2737.1.

Thompson, A. F., A. Lazar, C. Buckingham, A. C. Naveira Garabato, G. M. Damerell, and K. J. Heywood, 2016: Open-Ocean Submesoscale Motions: A Full Seasonal Cycle of Mixed Layer Instabilities from Gliders. *Journal of Physical Oceanography*, **46 (4)**, 1285–1307, doi:10.1175/JPO-D-15-0170.1, URL https://doi.org/10.1175/JPO-D-15-0170.1http://journals.ametsoc.org/doi/10.1175/JPO-D-15-0170.1.

Thompson, L., 2000: Ekman layers and two-dimensional frontogenesis in the upper ocean. *Journal of Geophysical Research: Oceans*, **105 (C3)**, 6437–6451, doi:10.1029/1999JC900336, URL https://doi.org/10.1029/1999JC900336http://doi.wiley.com/10.1029/1999JC900336.

Visbeck, M., 2002: Deep Velocity Profiling Using Lowered Acoustic Doppler Current Profilers: Bottom Track and Inverse Solutions*. *Journal of Atmospheric and Oceanic Technol-*

ogy, **19 (5)**, 794–807, doi:10.1175/1520-0426(2002)019⟨0794:DVPULA⟩2.0.CO;2, URL https://doi.org/10.1175/1520-0426(2002)019{\%}3C0794:DVPULA{\%}3E2.0.CO2http://journals.ametsoc.org/doi/abs/10.1175/1520-0426{\%}282002{\%}29019{\%}3C0794{\%}3ADVPULA{\%}3E2.0.CO{\%}3B2.

Wenegrat, J. O., and M. J. McPhaden, 2015: Wind, Waves, and Fronts: Frictional Effects in a Generalized Ekman Model*. *Journal of Physical Oceanography*, **46 (2)**, 371–394, doi:10.1175/jpo-d-15-0162.1.

LIST OF TABLES

TABLE 1. Values for scalars, velocities, and their gradients resolved at different observational scales.

	AVISO	SEASOAR	TRIAXUS	FLOAT
SCALES	>100 km	12 km	5 km	0.5 km
ζ	$0.03f\ \mathrm{s}^{-1}$	$0.15f\ \mathrm{s}^{-1}$	$0.7f\ \mathrm{s}^{-1}$	–
δ	$0.001f\ \mathrm{s}^{-1}$	$0.03f\ \mathrm{s}^{-1}$	$0.7f\ \mathrm{s}^{-1}$	–
α	$0.10f\ \mathrm{s}^{-1}$	$0.13f\ \mathrm{s}^{-1}$	$1.2f\ \mathrm{s}^{-1}$	–
$\nabla_h b$	–	$0.32\times10^{-6}\ \mathrm{s}^{-2}$	1.4×10^{-6}	–
KE	$0.12\ \mathrm{m}^2\ \mathrm{s}^{-2}$	$0.27\ \mathrm{m}^2\ \mathrm{s}^{-2}$	$0.27\ \mathrm{m}^2\ \mathrm{s}^{-2}$	–
w	–	$5\times10^{-5}\ \mathrm{m\ s}^{-1}$	$20\times10^{-5}\ \mathrm{m\ s}^{-1}$	$100\times10^{-5}\ \mathrm{m\ s}^{-1}$

LIST OF FIGURES

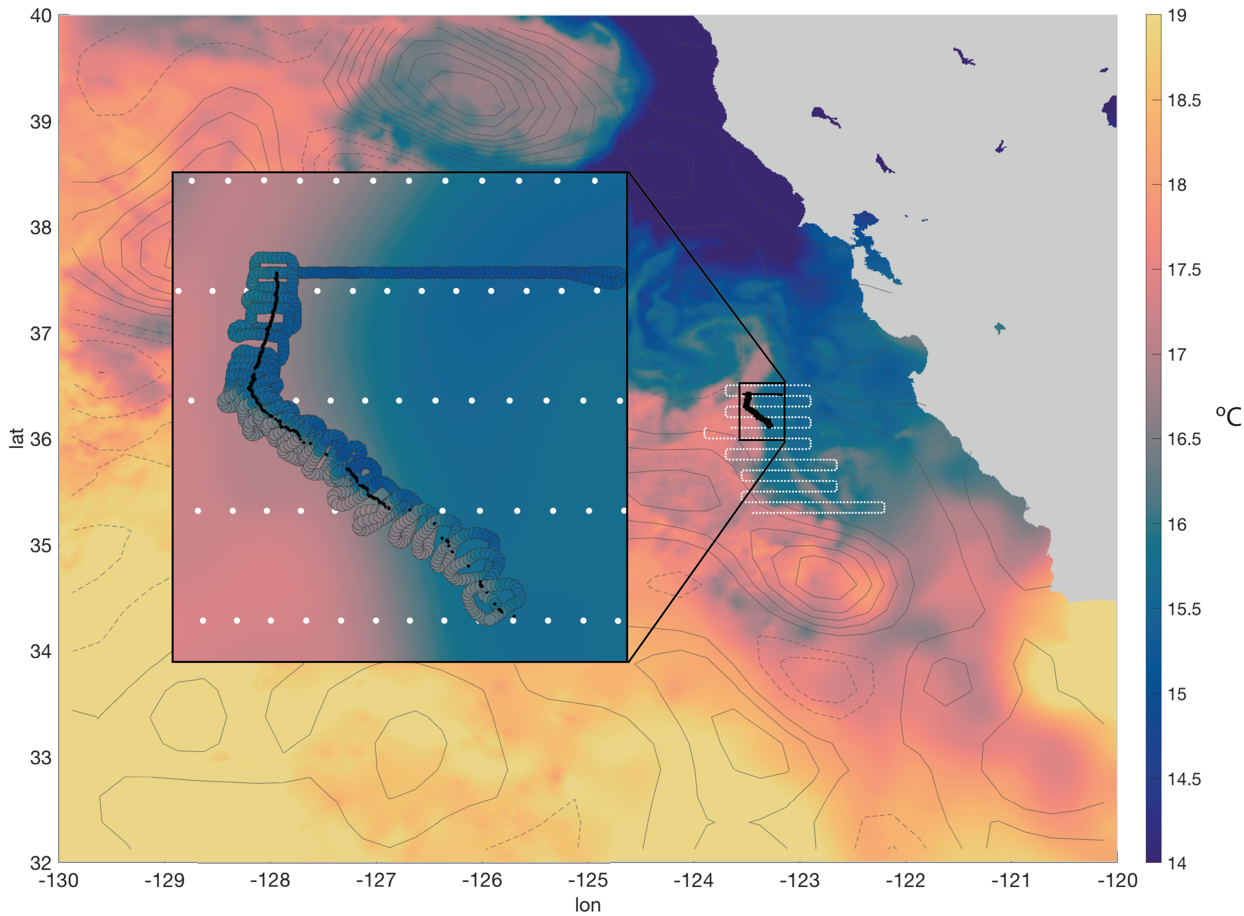

FIG. 1. SST off the California Coast on 4 August 2006 from the Group for High Resolution SST (GHRSST - https://podaac.jpl.nasa.gov). Contours are AVISO positive (solid) and negative (dashed) mean sea level anomaly. White dots outline the mesoscale survey ship track described in Pallàs-Sanz et al. (2010b); Johnston et al. (2011). Block dots outline the Lagrangian survey ship track. Inset) Detail of sea surface temperature (SST), the mesoscale survey (white), and the Lagrangian float track (black dots). The ship track is colored with ship underway temperature.

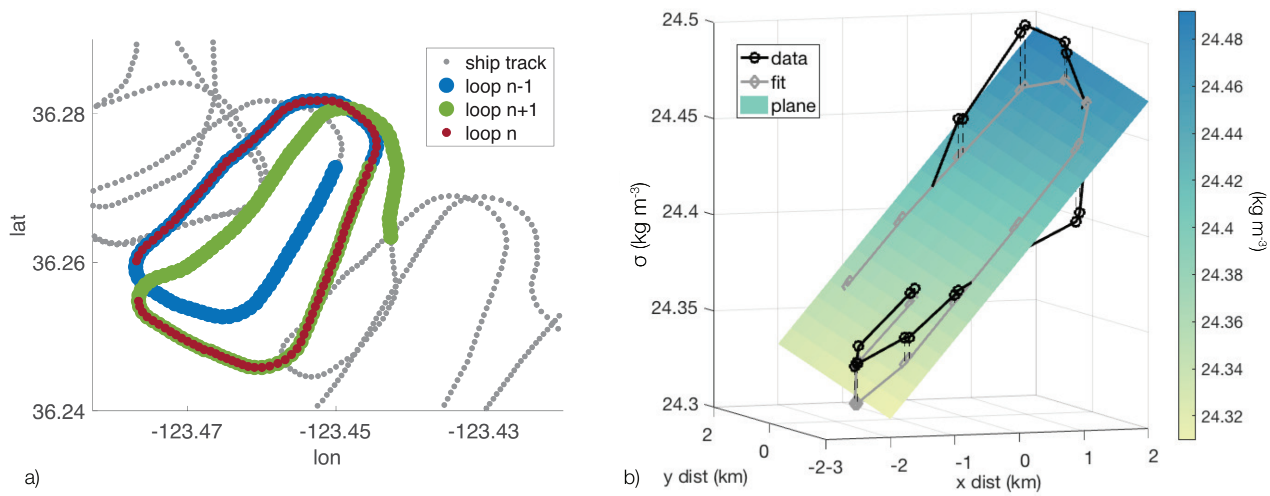

FIG. 2. a) Example of loops from underway data. A plane was fit to each loop, e.g. n1 (blue), n (red), and n+1 (green). Values from each plane fit were averaged together to form a single value for n. Each loop contained one hour of data, therefore each value for n contained two hours of data. b) An example plane fit to potential density over one loop of Traixus data at 4 m. Black circles are the observed data, and grey circles are projections of the observations onto the plane fit (1). The difference between the grey and black dots were used to estimate 95% confidence interval, ε in (2).

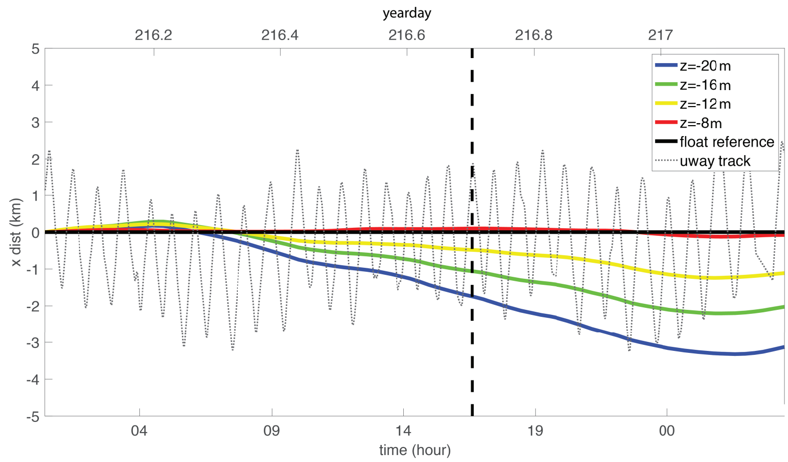

865 FIG. 3. Lagrangian analysis - Deformation distance at depth from initial volume. x-dist is the cross-frontal distance in the reference frame of the float as a function of time. The dashed line is the ship track, where each zigzag in time represents one loop. Colored lines are d^{xf} as described in section 2 and represent the distance a particle of water at depth z has been advected relative to the float. This can be used to assess the Lagrangian assumption of the survey. For example, at yd=216.7 (dashed line), d^{xf} implies that flow at 20 m is no longer true to the Lagrangian reference set at the beginning of the survey. While flow at 8 m is considered in the Lagrangian reference frame throughout the span of the observations.

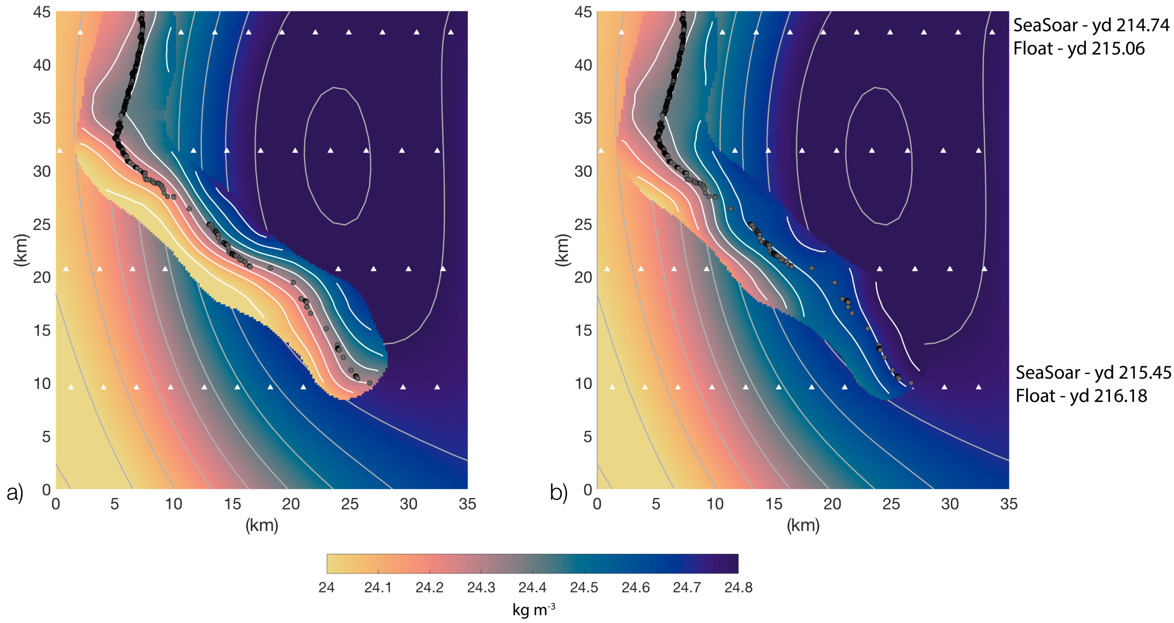

FIG. 4. Objective maps of potential density for the mesoscale survey at 16 m (background) in both a) and b), and the Lagrangian survey (foreground) at a) 4 m and b) 16 m). Distances are meridional (y-axis) and zonal (x-axis). Contours outline isopycnals every 0.1 kg m^{-3}. The float track (grey dots) and SeaSoar transect (white triangles) are included for reference. Yearday at two latitudes show time separation between the mesoscale and Lagrangian surveys. The tightly looped Triaxus track has been excluded for clarity, refer to Fig. 1.

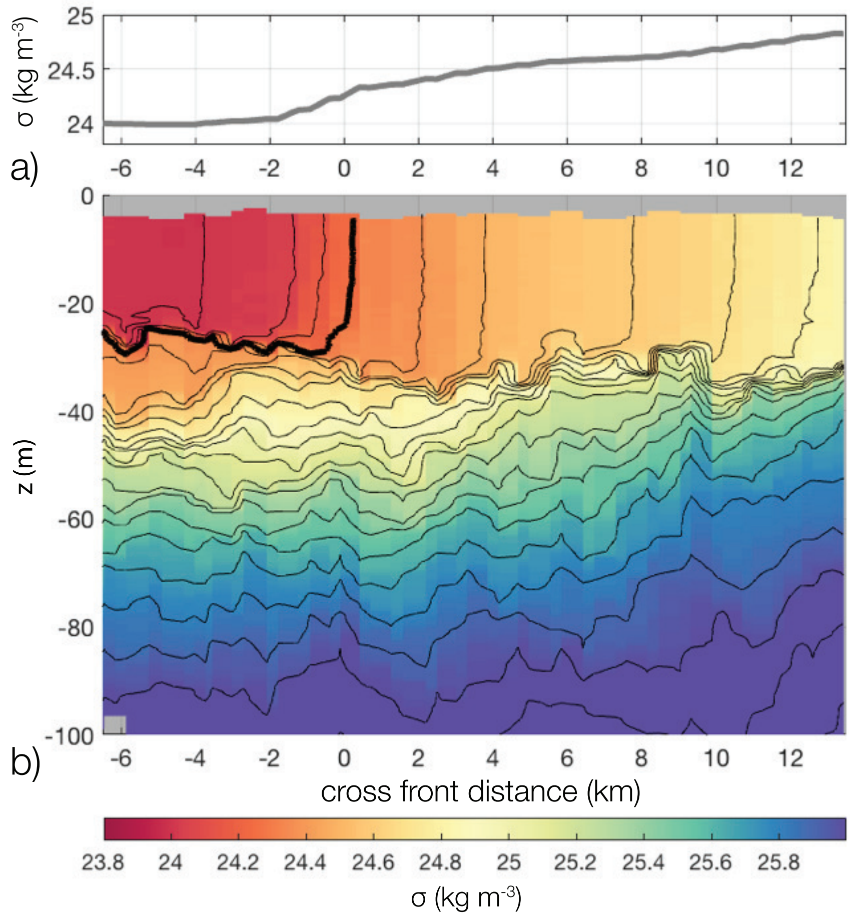

877 FIG. 5. Initial transect used to identity the front before placement of the float. a) cross-frontal potential density from the ship flow through system. b) cross-frontal potential density from Triaxus. Black lines are isopycnal contours of 0.1 kg m^{-3} and the dark black line is the 24.4 kg m^{-3} isopycnal.

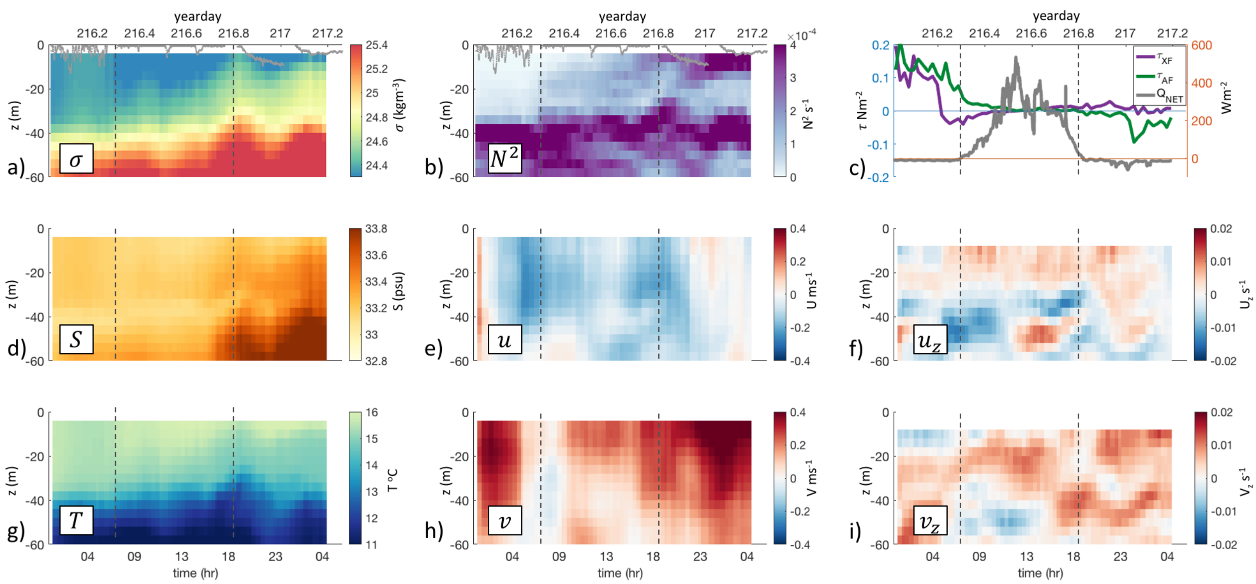

FIG. 6. Scalars and velocity of the front surrounding the float throughout the Lagrangian survey in depth and time. Values are means from the loops (see section 2). a) potential density and float depth (grey dots); b) N^2; c) along-front wind stress (green) and cross-front wind stress (purple), Q_{NET} positive into the ocean (grey); d) salinity; e) zonal velocity u ; f) zonal shear u_z; g) temperature; h) meridional velocity v ; and i) meridional shear v_z. Dashed grey lines denote the three stages outlined in section 4.

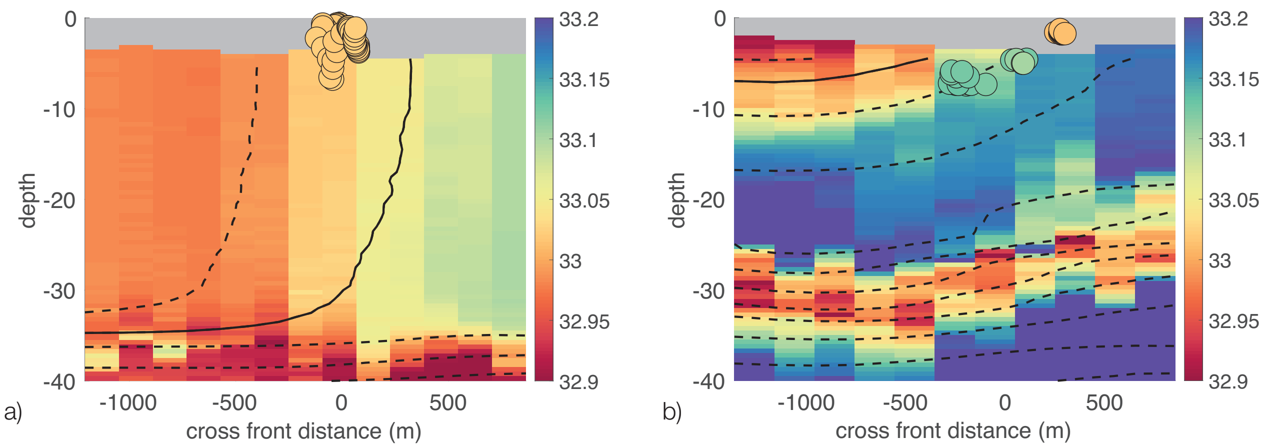

FIG. 7. Raw Triaxus salinity [PSU] a) at the beginning of the survey, stage 1, yd 216.1 and b) at the end of the survey, stage 3, yd 216.8. Potential density is contoured every 0.1 kg m^{-3} with the solid contour marking the 24.3 kg m^{-3} isopycnal. Circles denote the position of the float within $\pm$15 min of the transect and are colored by the average salinity measured by the float's sensors.

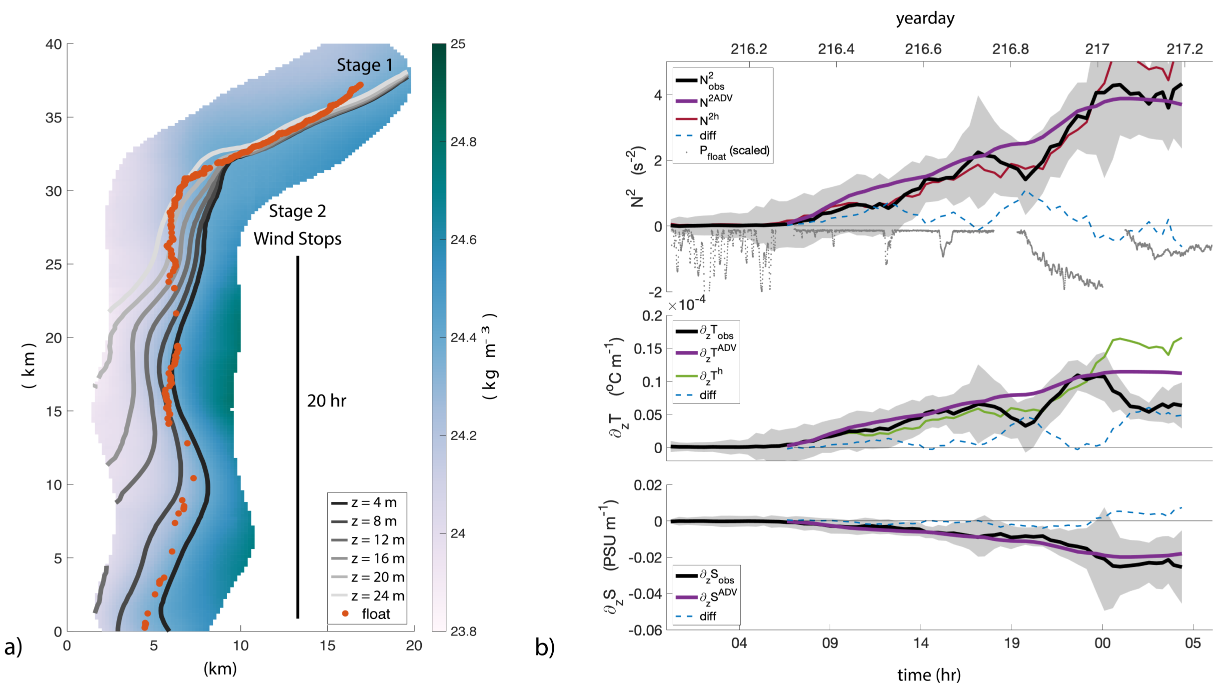

FIG. 8. a) Objective map of potential density at 4 m. The map has been rotated to follow the float trajectory (orange dots) during stages 2 and 3. The grey scale lines denote the 24.4 kg m^{-3} isopycnal at different depths. b) Vertical gradients discussed in section 4a. top to bottom: N^2, $\partial T/\partial z$, and $\partial S/\partial z$ at 8 m. Black lines are observations, purple lines are integrated values from (6). Blue dashed lines are the difference between the observations (black) and integrated (purple) values. The red line in the top plot is N^2 calculated from (3). Green line in the middle plot is estimated from (5). Scaled float depth is included for reference. Shaded regions are 95% confidence intervals (ε).

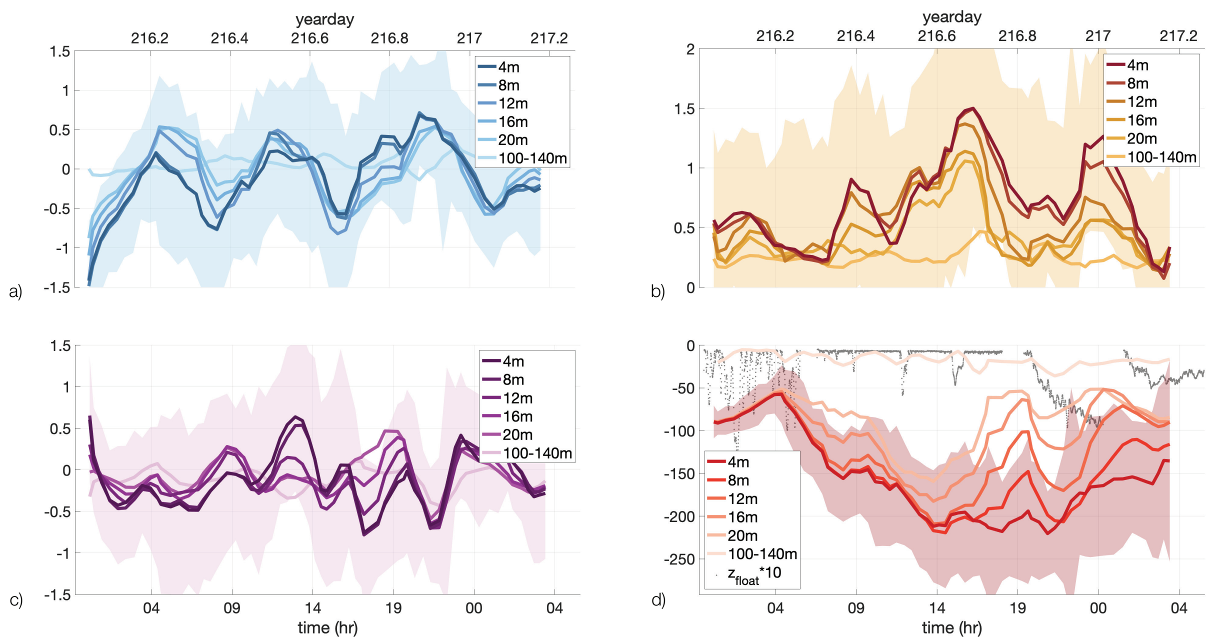

FIG. 9. (a) ζ/f, (b) α/f, (c) δ/f , and (d) $\nabla_h b/f^2$ plotted against time at depths 4 through 20 m and averaged between 100-140 m. Float depth scaled by $\times 10^3$ (grey dots) are included for reference. Shaded regions are 95% confidence intervals (ε) at 4 m.

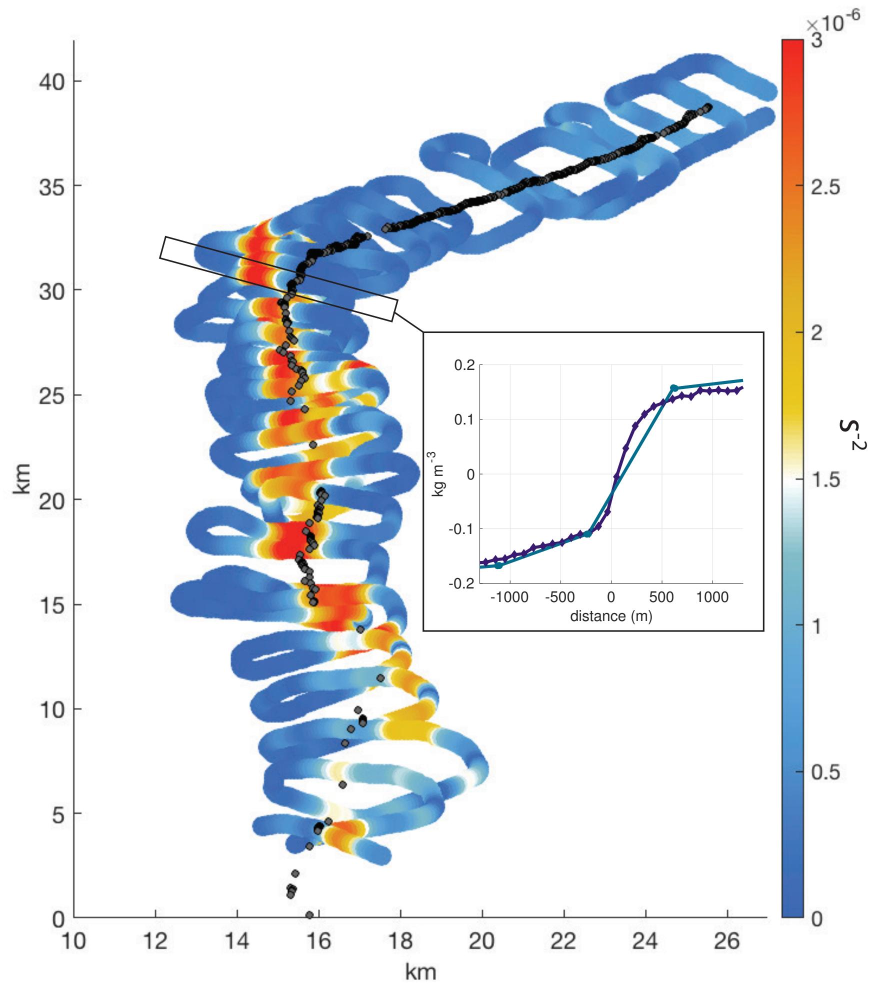

899 FIG. 10. $|\nabla_h b|$ [s^{-2}] calculated along the ship track (color) and float positions (grey dots) rotated along the average trajectory of the float during stage 2 and 3. Inset) example of a cross-front transect of potential density resolved by the underway (purple) and Triaxus at 4 m (blue).

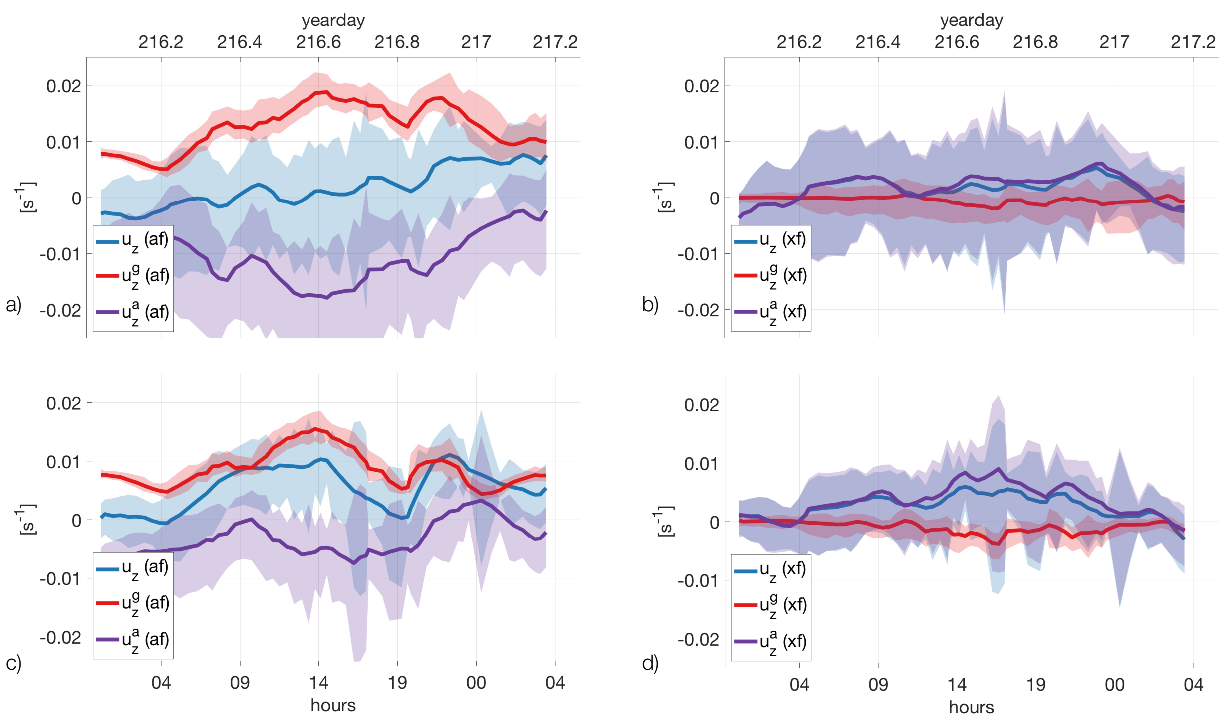

FIG. 11. Geostrophic shear, $\widehat{k} \times (\nabla_h b f^{-1})$ (red), ageostrophic shear (purple), and total shear (blue) for a) along-front (u_z^{af}) at 8 m, b) cross-front (u_z^{xf}) at 8 m, c) along-front (u_z^{af}) at 16 m, d) cross-front (u_z^{xf}) at 16 m. All terms have been rotated to align with $\nabla_h b$ at 4 m (section 2.2). Shaded regions are 95% confidence intervals (ε).

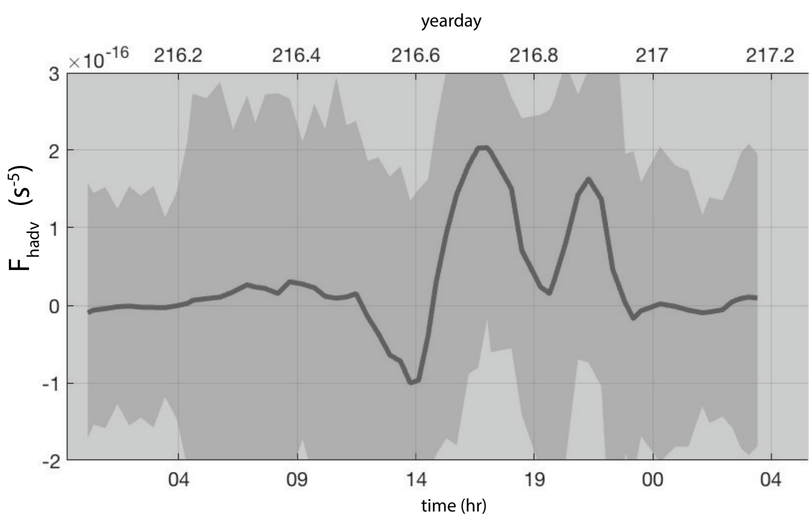

906 FIG. 12. Frontogenetic tendency (F_{hadv} [s^{-5}]) as a function of time at z = 8 m. Shaded regions are 95%
907 confidence intervals (ε).

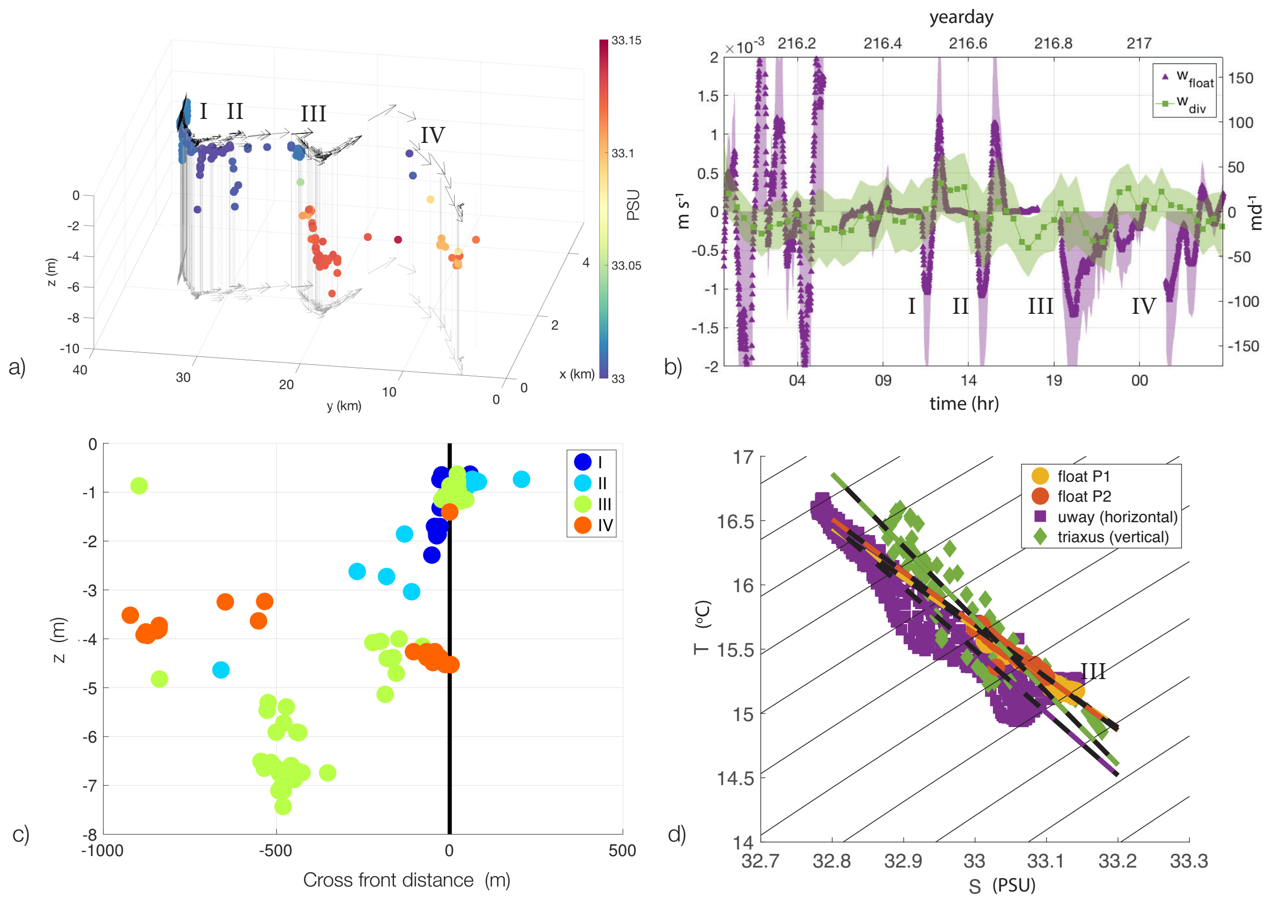

FIG. 13. Vertical velocity and float subduction. a) 3-D float subduction. The float's positions (circles) are colored by salinity. The float's trajectory is shown at the surface (black) and projected again at 10 m. Each float location and velocity vector is connected by a dashed grey line. b) Vertical velocity estimated directly from the pressure measured by the float (purple) and using the divergence calculated from Triaxus (green). c) Cross-frontal distance of the float as it downwelled under the front during events I–IV. d) $T-S$ diagram during downwelling events III. The float's two sensors (P1, yellow and P2, gold) and Triaxus (green) captured $T-S$ changes of the vertical stratification during the downwelling event, while the ship underway (purple) provided $T-S$ changes of the horizontal stratification. In all plots, downwelling events are labeled according to section 4e .

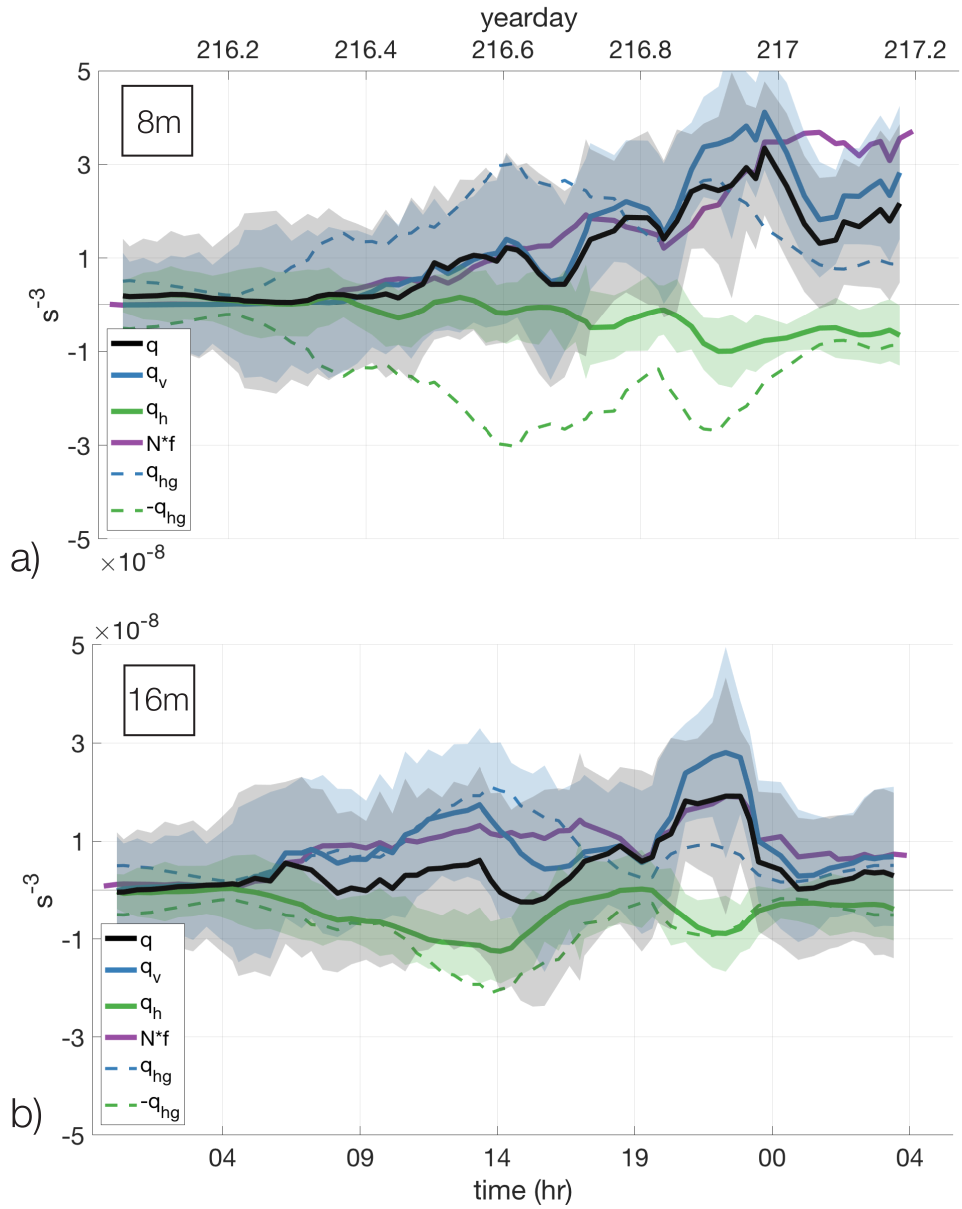

917 FIG. 14. PV (q, black), the vertical term of PV (q_v, blue) and the horizontal term of PV (q_h, green) at a) 8 m
918 and b) 16 m. Both plots include planetary PV ($N^2 f$, purple) and the horizontal term in PV if the flow were in
919 thermal wind balance (q_{hg}, dashed blue and $-q_{hg}$, dashed green). Shaded regions are 95% confidence intervals
920 (ϵ).